


2010-01-01

An Ab-Initio Study of the Elastic Properties of Important Group IV Diborides at High Temperatures

Manny Gonzales

University of Texas at El Paso, mgonzales1@gmail.com

Follow this and additional works at: https://digitalcommons.utep.edu/open_etd

 Part of the [Atomic, Molecular and Optical Physics Commons](#), [Materials Science and Engineering Commons](#), and the [Mechanics of Materials Commons](#)

Recommended Citation

Gonzales, Manny, "An Ab-Initio Study of the Elastic Properties of Important Group IV Diborides at High Temperatures" (2010). *Open Access Theses & Dissertations*. 2686.
https://digitalcommons.utep.edu/open_etd/2686

This is brought to you for free and open access by DigitalCommons@UTEP. It has been accepted for inclusion in Open Access Theses & Dissertations by an authorized administrator of DigitalCommons@UTEP. For more information, please contact lweber@utep.edu.

AN AB INITIO STUDY OF THE ELASTIC PROPERTIES OF IMPORTANT GROUP
IV DIBORIDES AT HIGH TEMPERATURES

MANNY GONZALES

Department of Mechanical Engineering

APPROVED:

Jack F. Chessa, PhD, Chair

Arturo Bronson, PhD

Murat Durandurdu, PhD

Chintalapalle Ramana, PhD

Patricia D. Witherspoon, PhD
Dean of the Graduate School

Copyright ©

By

Manny Gonzales

2010

AN AB INITIO STUDY OF THE ELASTIC PROPERTIES OF IMPORTANT GROUP IV
DIBORIDES AT HIGH TEMPERATURES

BY

MANNY GONZALES, B.S.M.E, B.S.M.M.E

THESIS

Presented to the Faculty of the Graduate School of

The University of Texas at El Paso

in partial fulfillment

of the requirements

for the degree of

Master of Science

Mechanical Engineering

THE UNIVERSITY OF TEXAS AT EL PASO

MAY 2010

PSALM 23

On preparing this thesis and during the beginning of my research, I found the doctoral dissertation of Peter David Haynes at the University of Cambridge. He included Psalm 8 right after his preface. I will follow suit, including Psalm 23, simply because it has become the kernel (As described by my good friend Ricardo Avila, who is mentioned in the acknowledgements) of western civilization. Ricardo once told me that if there was one thing that he wanted his students to memorize once they got out of his class (he usually teaches strength of materials), that was it. It took me a bit of time to realize *why* these simple words have become so crucial to the current system.

Although I find many of the proverbs of Benjamin Franklin or the Proverbs of Hell in William Blake's awesome work "The Marriage of Heaven and Hell" to be better suited for practice by man (and of greater spiritual and practical value to me), I believe it is important to know of this Psalm for the reasons mentioned above.

This version is quoted from the New international version of the bible, but the first line holds the key to unraveling a huge puzzle that has, for many years, troubled me to the point of anguish.

1 The LORD is my shepherd, I shall not be in want.

2 He makes me lie down in green pastures, he leads me beside quiet waters,

3 he restores my soul. He guides me in paths of righteousness for his name's sake.

4 Even though I walk through the valley of the shadow of death, I will fear no evil, for you are with me; your rod and your staff, they comfort me.

5 You prepare a table before me in the presence of my enemies. You anoint my head with oil; my cup overflows.

6 Surely goodness and love will follow me all the days of my life, and I will dwell in the house of the LORD forever.

ACKNOWLEDGEMENTS

This thesis culminated from work previously started in 2005 with Arturo Bronson and Jack Chessa at UTEP. With Jack's help, I was able to return during a turbulent period in my life and begin my academic enterprise anew. I owe Jack many thanks for his support. Art's many fruitful discussions and friendship helped make the experience memorable. To these two fellows, I give my full appreciation.

On returning to UTEP, I had the opportunity to teach Mechanical Engineering Lab I. I restructured the course and wrote a lab manual. This intellectually enriching experience I owe to Jack. Thanks for giving me the opportunity!

Dr. Stephen W. Stafford in metallurgy was material to my current success, both in the past and present. He is an inspiration: a true professor in every sense of the word, conforming above and beyond to Walter Noll's definition. There will be a time when I will become his successor. That blasphemous prophecy is one I know will come to pass.

Ricardo Avila, one of my only friends in this life, spent a lot of time with me in the fall semester, 2009. We let time pass and as it did, I found out that we shared much in common in our experience and perceptions. I really knew that to be the case long ago, but it is always a joy to find someone of like mind in the world. For his friendship, I give my thanks and a pledge of loyalty, one that goes beyond that of the standard connotation of the age in which we live.

In life, we seek only to find nurture among our fellow man. Most of the time, we instead find a cold and lonely place. The words of David Gold resound in my mind as many of the events that transpired in his life closely parallel those of mine. He decided to express them simply, yet eloquently in song. Two stanzas in particular are significant, and the notion of their existence merits my thanks to him. We share similar pain, and in that I managed to find a semblance of comfort during a time when the world showed its true form to me.

The first:

It is the discomfort that sets us apart

That wakes us up, that puts us to sleep

It is our pathetic moments

Which make us desire to be great

It is the starving itself

That makes us hungry to want more

Over time as you learn to fall

You'll rise to your feet faster than the time before

The second:

... It's no one's dream to follow me,

When everyone wants to be followed themselves.

Your self-expression is a reflection of the mind.

Use it to make your peace with yourself,

Those around you and the age in which you live.

Lastly, I wish to thank my mother, whose unwavering support has helped me reach these heights. She has sacrificed much for me, and I am happy to do the same.

I have adapted a mantra for living. It was spoken again in song by Ihsahn and his wife Ihriel in an aptly named piece: "The Moribund People." It explains much and I find joy sharing it with anyone reading this work.

Some suffer to the point where they grow numb.

Others are so numb, they deserve to suffer.

If anyone reached this point in their reading, my praise to you.

-MG

Contents

1	Introduction: The Need for New Materials in Extreme Environments	1
1.1	The Ultra-High Temperature Ceramics (UHTCs)	2
1.1.1	The group (IV) diborides	4
1.1.2	Typical microstructures	5
1.1.3	Mechanical Properties	8
1.2	Manufacturing Routes for UHTCCs	10
1.2.1	Synthesis Paths	10
1.2.2	Densification	12
1.2.3	Experimental Limitations	13
1.3	Modeling Techniques	13
1.3.1	Continuum Modeling	14
1.3.2	Molecular Ab Initio Modeling	16
1.4	Purpose and Scope of This Study	17
1.4.1	Outline of thesis	18
2	A review of past work in ab-initio modeling of UHTCs	19
2.1	Research into the manufacturing of UHTCs	19
2.2	Experimental studies of the mechanical behavior of group IV diborides . . .	20
2.2.1	Single Crystals	20
2.3	Ab-initio studies	22

2.3.1	Density Functional Theory studies	22
2.4	Recent developments	23
2.5	The approach of this study	24
3	Mathematical theory of the ab-initio methods: Density functional theory	25
3.1	The probabilistic nature of quantum mechanics	25
3.2	Dirac Notation	28
3.3	The Schrödinger equation	31
3.4	The tractability of quantum mechanics	33
3.4.1	The Born-Oppenheimer Approximation	33
3.4.2	The modified Schrödinger equation	35
3.5	The seminal works of Hartree, Hohenberg, and Kohn	36
3.5.1	Hartree-Fock Theory	37
3.6	The exchange-correlation terms	39
3.6.1	Density Functional Theory - Approach	40
3.7	Density Functional Theory - Implementation	40
3.7.1	Basis sets	43
3.7.2	Pseudopotentials	45
3.7.3	Exchange and correlation functionals	46
3.7.4	Self-consistent field calculations	47
3.7.5	Density Mixing	49
3.8	Summary	50
4	Ab-initio molecular dynamics and its application to the group IV diborides	51
4.1	Classical Lagrangian and Hamiltonian dynamics	51
4.2	Classical Molecular Dynamics	53
4.2.1	Deriving Properties	54
4.3	The Ab-initio Formulation	55

4.3.1	Born-Oppenheimer Dynamics	55
4.3.2	Ensembles	56
4.3.3	Temperature and Pressure Control	57
4.4	Conclusion	60
5	Methodology	62
5.1	Building the models	62
5.1.1	Lattice parameter refinement	63
5.2	Initial parameter setup for MD analysis	65
5.3	MD simulation specifics	67
5.4	Conclusion	69
6	Findings and Discussions	70
6.1	Results for the ZrB ₂ Lattice	70
6.2	Results for the HfB ₂ Lattice	78
6.2.1	Supercell	80
6.3	Results for the TiB ₂ Lattice	81
6.4	Summary	84
7	Conclusions and future work	87
	References	89
	Curriculum Vitae	98

List of Tables

4.1	A look at the different statistical ensembles.	58
5.1	The equilibrium lattice constants of the group IV diborides.	63
5.2	Input parameters for initial geometry optimization.	64
5.3	The equilibrium lattice constants of the group IV diborides after geometry optimization.	65
6.1	The elastic constants of ZrB_2 at elevated temperatures.	77
6.2	The high-temperature elastic constants of HfB_2 at elevated temperatures . .	80
6.3	The high-temperature elastic constants of TiB_2 at elevated temperatures . .	82

List of Figures

1.1	A snapshot of the various ceramics, some encompassing the UHTC family. Adapted from [16].	3
1.2	Reactive hot pressed microstructure of ZrB_2 -SiC ceramic at 1650°C [16]. Some void space is clearly visible. The darker phase corresponds to SiC.	6
1.3	(a) Fracture surface and (b) reactive hot pressed microstructure of HfB_2 -SiC ceramic. The darker phase corresponds to SiC. Predominantly intergranular fracture is observed, with SiC particles segregated at HfB_2 grain boundaries. Secondary phases of (1) HfC and (2) HfO_2 are also observed in the microstructure. Adapted from [52]	6
1.4	SEM micrograph of sintered TiB_2 at 2073 K using self-propagating high temperature synthesis. Uniform grains are present with distributed secondary particles at grain boundaries. Adapted from [92].	7
1.5	Microstructure of a BTM10 composite after being hot pressed at (a) 1850 and (b) 1950°C . Adapted from [30].	7
1.6	SEM image of a $\text{ZrB}_2/\text{ZrC}/\text{Zr-Si}$ composite obtained by reacting Zr-Si liquid with B_4C . ZrC and ZrSi_2 platelets with definite morphology are observed in a Zr-Si matrix. This is an example of a metal-matrix composite with ceramic reinforcement. Adapted from [75].	8

1.7	Complex microstructure of a ceramic composite with pronounced lenticular features and dispersed platelets. Particulate reinforcement with globular ZrO_2 is observed. A ZrO_2 scale and SiO_2 scale (not shown) provide oxidation protection. Some interfacial cracking near the scale is observed. Adapted from [75].	9
2.1	Dependence of Young’s modulus on crystallographic orientation for two different temperatures for CrB_2 , TiB_2 , and ZrB_2 . Adapted from [62].	21
3.1	Plane waves representing energy levels beyond a certain cutoff are neglected. The radius of the sphere is proportional to the cutoff energy set during pre-processing. Adapted from [1]	44
3.2	Schematic of the reformulation of the potential and wavefunction with a smoother pseudopotential. Adapted from [71]	46
5.1	The three diboride crystals which are the focus of this study.	63
5.2	The $P6/mmm$ space group that all diborides share. There are alternating networks of boron and metal atoms. Adapted from [16].	64
5.3	A conventional unit cell of ZrB_2	66
5.4	The HfB_2 supercell used to confirm the findings from Milman [48] that a single unit cell should be sufficient to track the properties of the system.	67
6.1	The data from Okamoto’s recent work [62].	71
6.2	Temperature fluctuations for the 2000 K ZrB_2 simulation are high when the Nosé q-ratio is set to 1.0. However, this temperature equals 2000 K on taking the ensemble average. The standard deviation is predicted by formula (6.1).	72
6.3	Temperature fluctuations for the 2000 K ZrB_2 simulation decrease when adjusting the Nosé-Hoover mass accordingly. The standard deviation is unchanged, however.	73

6.4	Pressure fluctuations for a 273 K ZrB_2 simulation are stable between about ± 15 GPa. Lower pressure fluctuations are expected for larger supercell simulations.	74
6.5	Pressure fluctuations are larger for a 1273 K simulation. The period of oscillation is lower due to the greater variation in lattice size (larger lattice fluctuations) at higher temperatures.	75
6.6	NPT Hamiltonian for a 1673 K simulation. The Hamiltonian begins to diverge at around 1.5 ps due to a large time step for the chosen thermostatting parameters.	76
6.7	The NPT Hamiltonian is nearly constant for the 2000 K simulation for modified thermostat parameters.	76
6.8	Lattice parameter variation for the ZrB_2 lattice at room temperature. These variations, when stable, were used to determine the average lattice parameter for a particular temperature.	77
6.9	The elastic constants of ZrB_2 at elevated temperatures.	78
6.10	Lattice parameter fluctuations for HfB_2 at 2200 K oscillate about a well-defined mean.	79
6.11	The elastic constants of HfB_2 at elevated temperatures.	80
6.12	Lattice parameter fluctuations for a single HfB_2 unit cell at 2200 K oscillate about a well-defined mean. The oscillations are stable for a simulation time of over 2.5 ps.	81
6.13	Lattice parameter fluctuations for HfB_2 supercell at 2200 K show stable oscillations. The oscillation range is smaller in comparison with figure 6.10. However, the mean value for the lattice parameters is surprisingly close ($\pm 0.3\%$).	82
6.14	The temperature fluctuation for a 2000 K TiB_2 simulation.	83
6.15	Pressure for the 2000 K simulation oscillates between ± 20 GPa.	83

6.16	The NPT Hamiltonian remained constant about a small range, as expected for conservation of energy.	84
6.17	The lattice parameters for TiB_2 at 2000 K show shorter fluctuations about a smaller mean value than the ZrB_2 and HfB_2 crystals at the same temperature.	84
6.18	The elastic constants of TiB_2 at elevated temperatures. Data shows excellent correlation with Okamoto's work [62] with a clear monotonic decrease in elasticity with increasing temperature. Data is underestimated due to the GGA approximation [48].	85

Chapter 1

Introduction: The Need for New Materials in Extreme Environments

The current thrust toward extra-lunar exploration necessitates the introduction of novel materials systems capable of withstanding highly taxing conditions. Applications such as atmospheric re-entry vehicles, leading edges, and coatings for end-stage turbine components rely on materials that can provide reliable, robust service without the need for constant maintenance, thus reducing downtime and cost. The integrity of such structures necessarily depends on the structure-property relationships of the materials at interfaces and any structure mismatch that may lead to a greater stress condition than normally experienced. Consequently, the material properties of these new materials must be carefully studied before the materials are put into service.

Composite materials provide a promising new paradigm in engineering design. By combining the properties of individual materials, composites exploit the favorable properties of each constituent while attempting to downplay any weaknesses each constituent may bring to the table. An interface forms when two dissimilar materials are joined as a natural consequence of the processing. Naturally, the interfaces between constituent materials play a key role in the overall structural behavior of these composites.

This study explores various constituents of common ultra-high temperature ceramic composites from a first-principles point of view. Experimental limitations inhibit exploration of these materials at extreme conditions, such as high temperature or high chemical potential. These limitations may be circumvented through theoretical studies of the constituents at simulated conditions. The limitations of these theoretical and numerical studies are explored and the applicability of such to various systems is outlined in what follows. This study only explores the elastic behavior of single crystals of various group IV diborides at elevated temperatures without consideration of phase transformations under pressure. The methods employed can be extended to other materials systems with relative ease.

This chapter focuses on the materials systems explored in this study. The typical manufacturing processes for these systems are outlined and a general introduction to the analysis techniques available to probe these systems is provided. The difficulties in manufacturing these systems and their potential applications are discussed in detail. Lastly, an overview of various numerical techniques is presented, with particular emphasis on the first-principles techniques which make up the bulk of this study.

1.1 The Ultra-High Temperature Ceramics (UHTCs)

Considerable research efforts have been placed on determining the optimal microstructural configuration of group (IV) ceramics, especially the borides and carbides. The extremely high melting temperatures of these ceramics place them in a category all of their own and are commonly referred to as Ultra-High Temperature Ceramics and Ceramic Composites (UHTCCs). The relative chemical stability, ablation resistance, and corrosion resistance of composites composed of ZrB_2 in particular make these materials attractive as protective coatings for components in extreme environments, such as in re-entry vehicles and rocketry [64, 29, 90, 93]. The superb thermal shock resistance and chemical stability in the presence of molten metals make ZrB_2 an obvious candidate for applications in these extreme

environments [56, 40].

Figure 1.1 gives the melting temperatures of various well-known ceramic materials, many of which go beyond the threshold temperature recognized as the UHTC demarcation point. Many UHTCs belong to borides and carbides of various transition metals, including those of group IV. Some important nitrides and even some well-known metals can be characterized by their ultra-high melting points. It is the relative chemical stability, specific density, and retention of high temperature strength of many of the important UHTCs that separate them from the ultra-high temperature metals. These properties make the UHTCs very attractive for use in the most demanding environments as coatings or even as monolithic components.

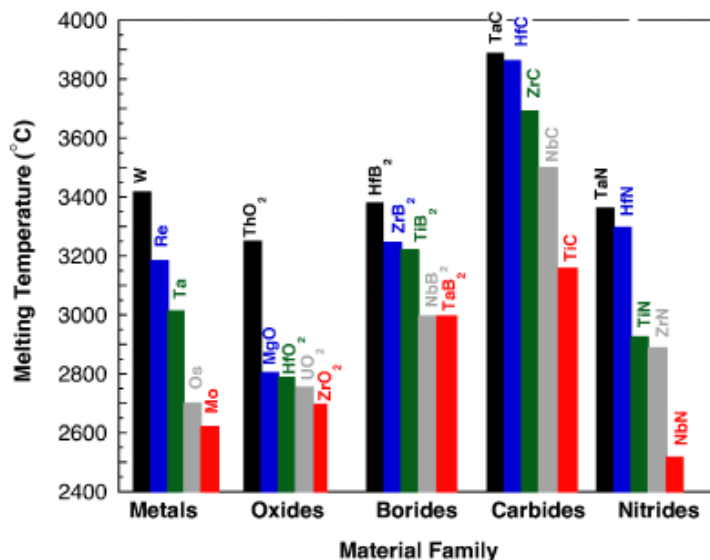


Figure 1.1: A snapshot of the various ceramics, some encompassing the UHTC family. Adapted from [16].

The microconstituents of UHTCCs are UHTCs themselves and can take on various morphologies depending on their processing. Morphologies range from globular to lenticular and thus the surface properties of these composites vary depending on the volume fraction of constituents and their relative distribution. The optimum microstructural state will depend on the processing and manufacturing route, as well as the volume fraction of each constituent. The solubility of the microconstituents with other transition metal borides will affect the mechanical and thermal properties appreciably [16]. However, the elastic properties will be

relatively immune to such phenomena, as the elasticity is an atomistic property [12].

1.1.1 The group (IV) diborides

The group (IV) refractory diborides exhibit unique material and chemical properties that make them attractive for use in high temperature conditions. Zirconium and hafnium diboride show excellent oxidation resistance and are chemically inert in the presence of various molten metals, making these materials attractive as refractory crucibles. These diborides also form partial solid solutions with other transition metal diborides, making these materials very flexible to tailoring of their properties [16].

The UHTCs have found use in high temperature applications such as refractory lining and crucibles for high temperature manufacturing [56] applications. The resistance to oxidation of ZrB_2 in particular has propelled its use as an electrode for furnace applications. TiB_2 has already found widespread use in armor and cutting tools due to its ablation resistance and high temperature strength. The low specific density of these UHTCs and their high-temperature stability in particular has accelerated the current research thrust toward understanding the fundamental mechanisms driving the behavior of these materials systems.

The manufacturing process typical of creating monolithic UHTCs is that of hot pressing, which yields simplistic geometries. High purity particles of the ceramic are consolidated via hot-pressing and a solid state adhesion process known as sintering takes place at kinetically favorable (high temperature and low oxidation potential) conditions. Reactive means of processing exist where through a carbothermal reduction; a liquid-phase boron compound reacts with ZrO_2 in a carbonaceous atmosphere to yield ZrB_2 by redox. Reactive hot pressing and sintering are also common synthesis routes to creating monolithic UHTCs [3]. Other more advanced techniques include spark-plasma sintering (SPS) and hot pressing with ceramic and polymeric precursors (See [16] for more details).

The greatest obstacle to creating complex parts of ZrB_2 and other group IV diborides is the densification of the part, i.e. the approach of the component to full theoretical density,

especially through conventional sintering processes. Speyer et al [38, 39, 11] showed through a fundamental study that a grain coarsening effect was responsible for inhibiting the sinterability of B_4C . Similar mechanisms may be responsible for the densification barriers in the group IV diborides [16]. Solid solutions of metallic sintering aids have been cited to improve sinterability of ZrB_2 [96]. Ceramic precursors and SiC are commonly employed to improve densification during hot pressing. Much work still remains to be done in improving the manufacturability of monolithic components of these UHTCs.

1.1.2 Typical microstructures

Figure 1.2 shows a typical microstructure for reactive hot-pressed ZrB_2 . SiC additions promote sintering through a modification of surface energy between ZrB_2 particles. In addition, SiC and B_4C promote pressureless sintering of ZrB_2 , as outlined in [97, 98]. The secondary phase in these UHTCCs tends to segregate at grain boundaries due to preferential energetics [59, 77].

Similar microstructural features are appreciated from HfB_2 ceramics. Figure 1.3 shows a fractured surface of a reactively hot-pressed HfB_2 along with its polished photomicrograph. SiC particle of globular morphology are observed at HfB_2 grain boundaries. The fracture is intergranular along the grain boundaries, enhanced by the presence of SiC. TiB_2 shows similar microstructural features in comparison with HfB_2 , as shown in figure 1.4.

The UHTCCs are composed chiefly of UHTCs as matrix material with some thermally-stable reinforcement material, such as SiC fibers and particles. The thermal expansion mismatch between constituent interfaces will cause inherent eigenstrains (self-equilibrated strains) and residual stresses in the material [58]. The surface properties and energies are critical driving forces [59] to the chemical stability and inherent diffusivity in the material. Thus, a consideration of surface and mechanical properties is necessary when manufacturing such UHTCCs.

Figure 1.5 shows a ceramic matrix composite composite for the $B_4C/TiC/Mo$ system.

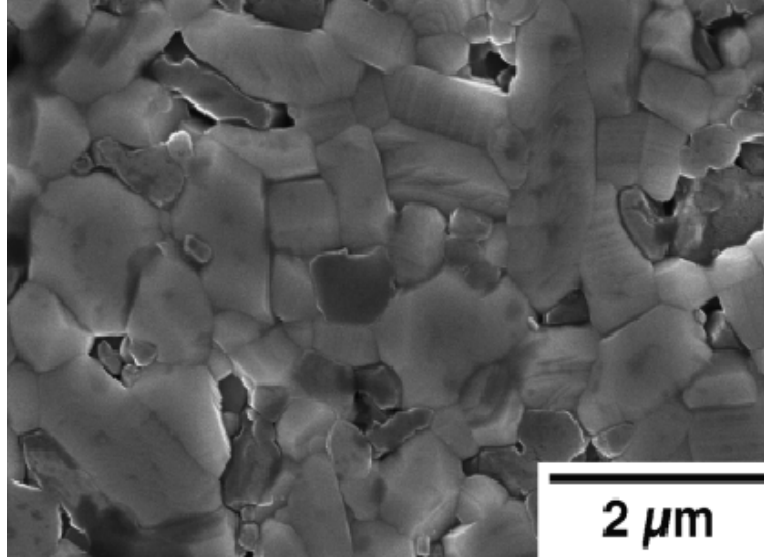


Figure 1.2: Reactive hot pressed microstructure of $\text{ZrB}_2\text{-SiC}$ ceramic at 1650°C [16]. Some void space is clearly visible. The darker phase corresponds to SiC.

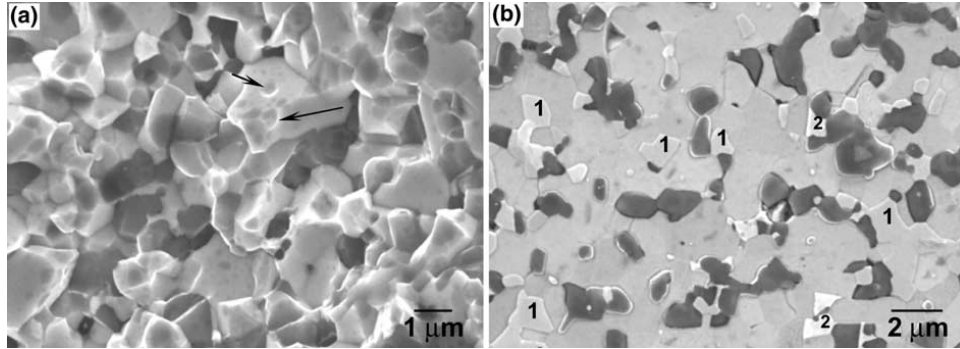


Figure 1.3: (a) Fracture surface and (b) reactive hot pressed microstructure of $\text{HfB}_2\text{-SiC}$ ceramic. The darker phase corresponds to SiC. Predominantly intergranular fracture is observed, with SiC particles segregated at HfB_2 grain boundaries. Secondary phases of (1) HfC and (2) HfO_2 are also observed in the microstructure. Adapted from [52]

Similar composites may be manufactured through reactive routes and hot pressing consolidated particles for the Zr and Hf systems. The reinforcement provided by the secondary phases on the ceramic matrix can improve strength and hot hardness while promoting improved toughness in certain cases [16].

Purely reactive routes for manufacturing complex composites were explored in [75] and [31], where a packed bed of B_4C served as the reacting agent with Zr particles based on the

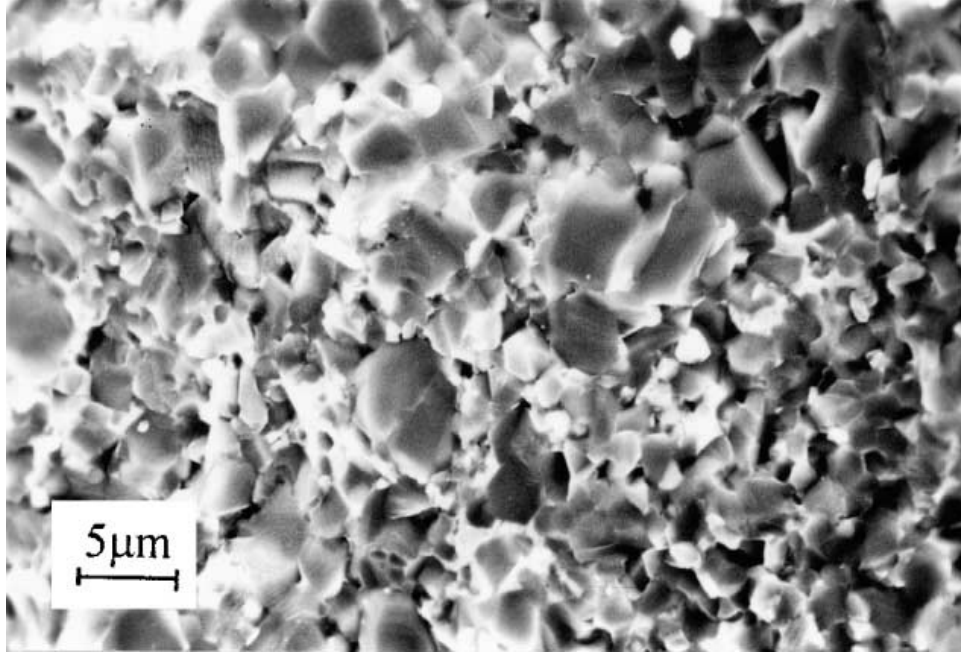


Figure 1.4: SEM micrograph of sintered TiB_2 at 2073 K using self-propagating high temperature synthesis. Uniform grains are present with distributed secondary particles at grain boundaries. Adapted from [92].

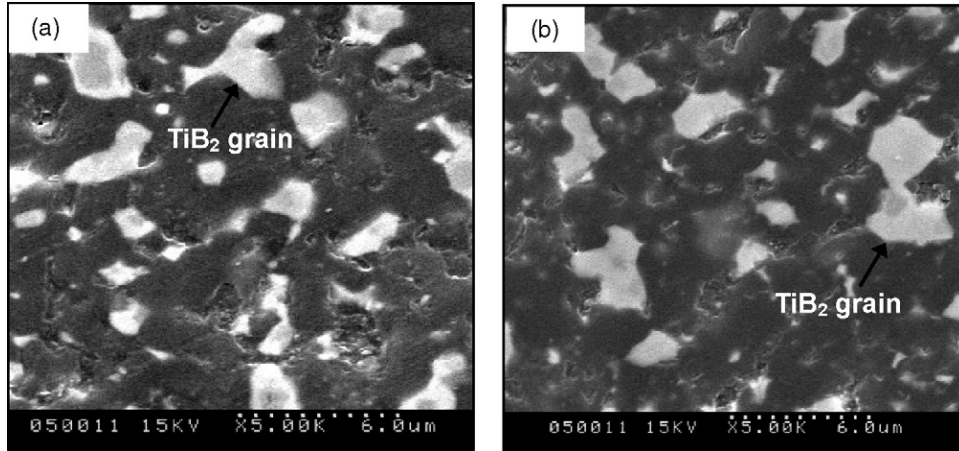
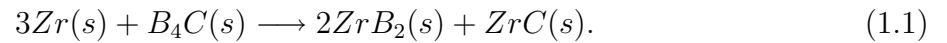


Figure 1.5: Microstructure of a BTM10 composite after being hot pressed at (a) 1850 and (b) 1950 °C. Adapted from [30].

reaction:



Typical microstructures for these reactions show a dispersion of secondary particle phases

with well-defined morphologies, as shown in figure 1.6. Oxidation potential of these materials is decreased with the aid of a protective oxide scale as shown in figure 1.7. These microstructures are very complex in contrast with the monolithic UHTCs (with perhaps marginal reinforcement with SiC), and represent the next step in the evolution of UHTCs.

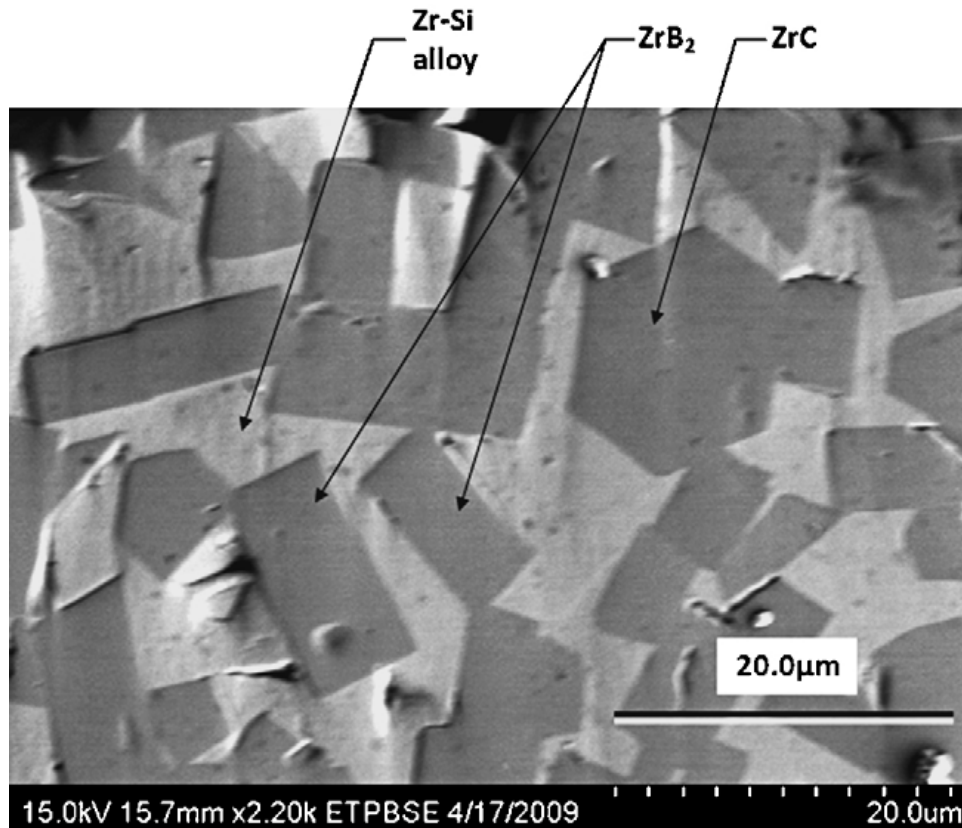


Figure 1.6: SEM image of a $\text{ZrB}_2/\text{ZrC}/\text{Zr-Si}$ composite obtained by reacting Zr-Si liquid with B_4C . ZrC and ZrSi_2 platelets with definite morphology are observed in a Zr-Si matrix. This is an example of a metal-matrix composite with ceramic reinforcement. Adapted from [75].

1.1.3 Mechanical Properties

The UHTCs exhibit very high strength and hardness as well as excellent ablation resistance and chemical stability. The strong covalent bond networks promote high hardness and the solid solubility of group IV diborides promotes a strengthening effect. Polycrystalline mechanical properties of monolithic diborides are readily available and are usually obtained

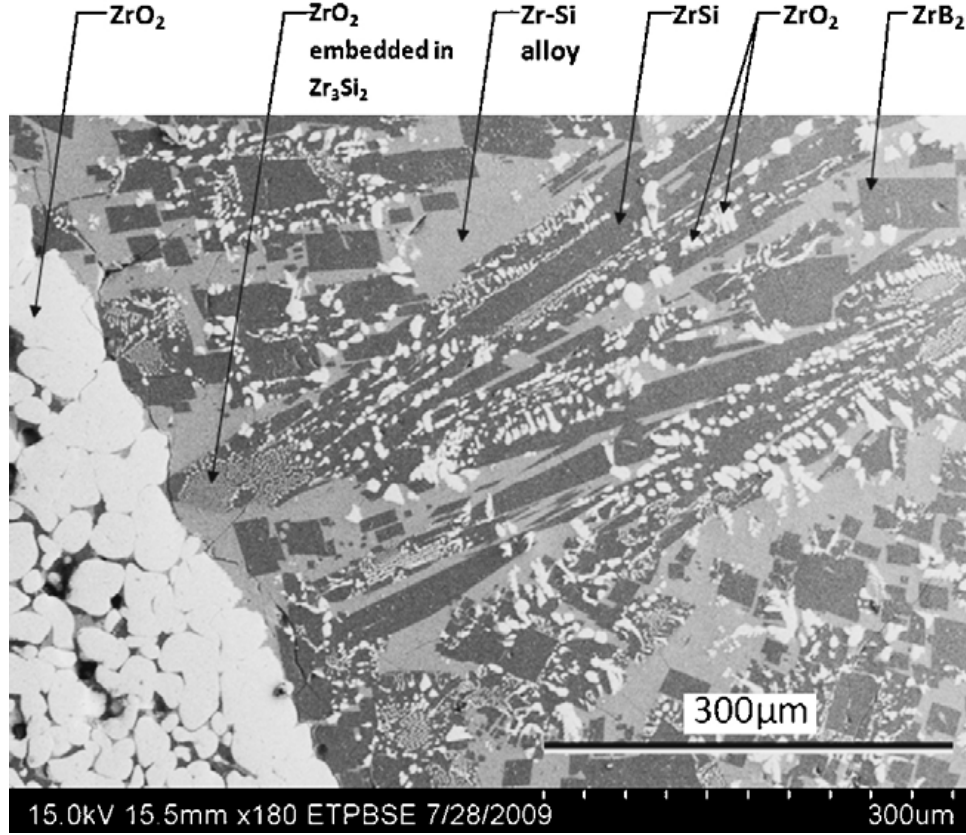


Figure 1.7: Complex microstructure of a ceramic composite with pronounced lenticular features and dispersed platelets. Particulate reinforcement with globular ZrO_2 is observed. A ZrO_2 scale and SiO_2 scale (not shown) provide oxidation protection. Some interfacial cracking near the scale is observed. Adapted from [75].

through bend tests and fracture toughness tests though microhardness [55, 95] Single-crystal properties are more difficult to obtain due to the inherently difficult manufacturing process.

The mechanical properties of single crystal ZrB_2 has been extensively studied by Okamoto [63]. These papers present mechanical data for single crystals of ZrB_2 obtained through a zone-refining process. A recent paper by [62] provides new data for ZrB_2 and other UHTCs. Monolithic ZrB_2 , in polycrystalline form, has been extensively studied and mechanical data is summarized in [16] among others. No systematic studies of HfB_2 single crystal elastic properties exist to the author's knowledge. This issue is further dealt with in chapter 2.

1.2 Manufacturing Routes for UHTCCs

The strength of the covalent bonding networks created in ZrB_2 provides a challenge to densification of the material. The distribution and chemistry of secondary phases produced during manufacturing are also of critical importance to the properties of the material. Traditional methods of densification include hot pressing, pressureless sintering, and spark plasma sintering (SPS)¹. Monteverde [53] provides an excellent review of the effects of the secondary phases formed during hot pressing on the mechanical properties.

Fahrenholtz [16] provides a summary of the common manufacturing routes for polycrystalline specimens of ZrB_2 and related composites. Chemical reduction provides a method of manufacture whereby the stoichiometric oxide of Zr may be reduced in the presence of carbon or B_4C . Aluminum may also act as a reducing agent in production. Chemical reactions may also be used to synthesize ZrB_2 , but discussion is deferred to [16]. Even simpler direct reactions involving the combination of boron and zirconium require control of the atmosphere due to the oxidation potential. These and other synthesis routes are discussed in section 1.2.1.

The densification of ZrB_2 becomes difficult because of the chemical bonding and low self-diffusion coefficients. The common routes for densification are discussed in section 1.2.2.

1.2.1 Synthesis Paths

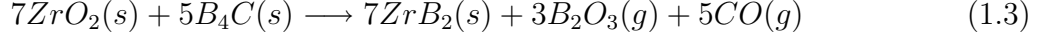
The carbothermal reaction commonly used in industrial processing of ZrB_2 takes ZrO_2 with a liquid-phase boria compound in a carbonaceous atmosphere [16, 88].



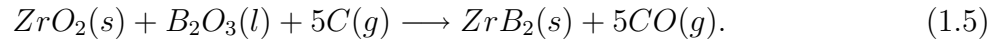
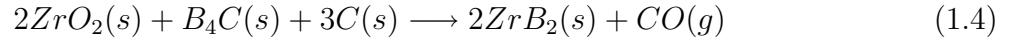
A simple thermodynamic calculation of the Gibbs free energy of formation shows the reaction to be highly endothermic and stable at around 1500°C . Excesses gases are produced that

¹Not discussed in this paper. See [2] for an excellent treatment of the subject

must be removed during reaction. Excess porosity is not uncommon as a result. A more thermodynamically favorable route involves the reduction of ZrO_2 in the presence of boron carbide B_4C :



where the reaction is stable at lower temperatures. Reduced oxide and carbon impurities are observed in this reaction due to the lower solubility of the compounds produced. The presence of B_4C has the added benefit of reducing the amount of oxygen present by reacting to produce boria as a by-product. Reduction routes for improved densification were studied extensively in [98], where added carbon and B_4C improved the relative density by removal of oxides from grain boundary triple points through active reduction based on:



Continued removal of the resulting gas phase through vacuum depends on the partial pressure of CO and the reaction conditions. Zhang et al [98] cite a partial pressure of 25 Pa, well below that of the produced vacuum in their experiments. The boria liquid phase has been shown to remain entrapped in micropores ² in residual form up to a concentration of 10%.

Direct synthesis routes:



prove useful as they are highly exothermic³ and can set off a self-propagating reaction, leading to a combustion synthesis of powders. Localized melting of Zr allows the synthesis with the

²Likely aided by surface tension and capillary action, as well as high surface energies related to the relatively large surface area of the particles

³Thermodynamically feasible at most operating temperatures

boron powders. This, however, creates large residual porosity and defects due to the large cooling rates involved. Oxidation potentials are large and the reactions must be carried out in controlled, inert atmospheres.

1.2.2 Densification

Densification of ZrB_2 composites has traditionally been ensured through hot pressing at large pressures and temperatures⁴ [16, 56]. Densification is likely due to a diffusion mechanism (sintering of particles), though the presence of a liquid phase may accelerate the reaction depending on wettability. This process leads to fully dense structures depending on the additions of different metals/compounds that aid in the reduction of the densification temperature. However, the presence of these additives proves detrimental to the mechanical properties of the material [16]. Furthermore, the grain size is closely related to the presence of oxide and compound additives present at interfaces of particles⁵. Morphology may be affected during grain coarsening as a result of evaporation of phases at high temperatures. This will eventually affect the overall mechanical properties of the monolithic material.

Pressureless sintering has been recently explored in [98], where chemical reduction reactions similar to those presented in section 1.2.1 demonstrate the removal of residual oxide phases by an excess of carbon as a reducing agent. The presence of carbon in resin form (after charring [98]) coats the ZrO_2 precursor particles, improving densification by inhibiting oxide formation at interfaces.

Fabrication of large components to near-net shape [16] becomes possible with this sintering route, in addition to being more cost-effective than hot pressing. Densification is enhanced by ensuring a small starting size for the precursor particles and by addition of various additives, including SiC (which has the additional benefit of improving flexural strength

⁴On the order of 30 MPa and 2000°C

⁵The driving forces behind full densification seem to be a reduction in the interfacial energies between particles during diffusion, which is inhibited by the presence of tramp compounds on the surfaces of particles. [16] cites an improvement in densification with the presence of oxides at interfaces, but showing a detrimental after-effect with grain coarsening and pore growth as by-products of these oxides

[98]. The presence of oxides enhances densification, which is attributed to surface reactions with liquid phases of boria, subsequently transforming to ZrB_2 , the more stable compound at the high sintering temperatures.

1.2.3 Experimental Limitations

The high melting temperatures of group IV diborides hampers the manufacturing of large single crystals. Furthermore, the inherent difficulty of elastic testing at elevated temperatures hampers any advancement in discerning accurate mechanical properties for these systems. Any systematic study of the microstructure of these materials under stress will require the elastic properties at elevated temperatures.

Limitations at high temperatures

Single crystal ceramics are limited in size and their purity is difficult to control. The floating-zone method has been used with success in synthesizing single crystals. Large-scale tensile specimens are currently impossible to produce due to these difficulties. Elastic properties are discernible with a surface wave propagation technique [63], whereby a surface wave allowed to propagate through the single crystal in a controlled atmosphere at elevated temperatures. The time-of-flight (tof) measurement of the wave provides the elastic constants based on solutions to the wave equation. These methods were employed in the only systematic study of ZrB_2 single crystals [63, 62]. This topic is treated in greater detail in chapter 2.

1.3 Modeling Techniques

Because of the experimental difficulties associated with mechanical testing and manufacturing of single crystals of group IV diborides, a numerical route shows promise in probing these materials under simulated conditions. A top-down approach may be taken whereby a monolithic component is studied in the macroscopic scale (a length scale on the order of

meters) and the effects of the microscale on the overall macrostructure are complementary in the analysis.

The modeling technique depends largely on the length scale being probed. Continuum modeling techniques rely on the assumption of material continuity so that calculus of single-valued functions may be employed in finding a closed-form solution to the problem. The problem may be formulated using these models and numerical techniques can be employed to come up with a good approximation. However, these models break down at length scales where the atomic (discrete) nature of matter interferes with the continuum hypothesis.

At this point, other techniques should be considered that can treat discrete particles while maintaining a statistical link with the larger scales. Here, the methods of statistical mechanics are joined with classical mechanics to approximate the behavior of matter in the large scale from data from the small scale. The behavior of the discrete matter is assumed to be governed by some conservative potential. The different methods of formulating such potential invariably lead to the ab-initio approaches, where the fundamental axioms (i.e. Schrödinger’s equation) are used to analyze the system.

1.3.1 Continuum Modeling

Continuum modeling of materials systems can refer to anything from micromechanical models describing average properties of materials, to numerical techniques that solve the partial differential equations of interest in finite domains, stitching together a solution for the entire domain of interest. The key factor in continuum modeling is that the material is idealized as a continuum. That is, the material is made up of a continuous set of material points and can be described by continuous functions, thus yielding to the techniques of the Calculus. While the structure of materials at the atomic level is well-known to be discrete, the sheer number of these atom at higher length scales “homogenizes” the structure leading to a continuous distribution (more or less) of atoms, thus making the continuum hypothesis valid.

Many continuum models exist that describe material behavior at the various length scales.

Micromechanics models exist where an inclusion or inhomogeneity in a homogeneous structure are modeled as eigenstrains (self-equilibrated strains arising as a result of the material response to external loads) in addition to the elastic strains arising from linear-elastic material behavior. Larger length scales have well-known continuum models that describe the behavior of homogeneous bodies with anisotropic properties. A body with a complex geometry will be very difficult to analyze in a closed-form employing some of these methods. For complex domains, numerical methods are the way to go.

Finite Element Modeling

The finite element method has been shown to be a robust numerical method in studying equations on arbitrarily shaped domains in a continuum. An arbitrary domain is meshed⁶ with a collection of elements that each have some kind of spatial variation associated with them. These elements are connected at points known as nodes and the solutions to the differential equations governing the behavior of some dependent variable are obtained in an averaged sense at the nodes through the finite element approximation.

The finite element method is derived from a variational statement of the problem leading to a weak formulation of the governing differential equations⁷. This weak formulation is discretized by a suitable method (the Bubnov-Galerkin method where the variational takes the form of the approximating function is typical) and matrix equations representing the variation of some field quantity are obtained. These equations are typically solved with numerical algorithms for matrix inversion, exploiting the inherent sparsity and topology of the matrices. The field variables at the nodes are used to stitch together a solution for the domain of interest using continuity conditions.

Various new extensions to the traditional finite element method have become popular for microstructural design [49, 86] by incorporating enrichment functions to the traditional

⁶By “meshed” I mean to say that the domain of interest is segmented into simple geometric shapes. These new domains are called “elements” and are of “finite” size, ergo finite elements.

⁷An integral form that relaxes continuity requirements for admissible functions describing the behavior of the dependent variable. See [28] for more details.

approximation functions of FEM and invoking the partition of unity principle [44]. These enrichments expand the solution space of traditional finite elements to capture any singularity or jumps in the field variable that could not otherwise be resolved. The added advantage of little or no remeshing as the singularities grow (cracks, for example) make these methods very attractive for predictive modeling and simulation of complex microstructures, especially at interfaces.

1.3.2 Molecular Ab Initio Modeling

In the molecular modeling techniques, the atoms and molecules encompassing matter are modeled as solid interacting spheres under the influence of some conservative potential field. This field may be semi-empirically derived (classical molecular dynamics) or is determined “on the fly” (ab-initio dynamics) using first-principles techniques. As described by Haile [23], molecular dynamics is a means to solve the many-body problem in classical mechanics. Thus, the discrete nature of matter is modeled as classically-behaving point particles governed by some potential field. Coupled with statistical mechanics and thermodynamics, the trajectories⁸ can provide many macroscopic and physical properties of the matter by considering the behavior of many (a statistically significant amount) particles.

Ab-initio literally means “from the beginning,” and thus encompasses all mathematical modeling techniques that solve the first-principles equations⁹ of a system using some kind of numerical approximation scheme.

Many quantum chemistry schemes such as the Hartree-Fock method can be considered ab-initio methods. Density functional theory is an ab-initio method that finds solutions to the Schrödinger equation by assuming that the energy of the system is a functional of the electron density. Furthermore, the first variation of the functional gives the ground state

⁸The trajectory shows the time-evolution of the phase-space, i.e. the positions and velocities of the particles in space

⁹All first-principles equations are treated as axioms where all other equations follow. Newton’s equations can be considered a classical first-principles form. Obviously those equations break down at the quantum level. The Schrödinger equation would be the quantum mechanical analog to the Newtonian equations of motion

(lowest energy state) based on the Hohenberg-Kohn theorems [26], so that the true structural state of the lattice is determined by a simple functional, rather than with the full multi-body formulation of the Schrödinger equation.

The crux of the ab-initio approach is to interrogate the system from the atomistic level, solving the Schrödinger equation through approximation and defining the system state through statistical ensembles, thus providing the behavior of a system at its most basic level. Many macroscopic interactions depend strongly on the behavior at length and time scales observable only through Quantum mechanical approaches. The ab-initio methods allow for many-body systems to be analyzed Quantum-mechanically, as our current mathematics are insufficient to analytically solve the coupled set of partial differential equations arising from the many-body Hamiltonian [70].

1.4 Purpose and Scope of This Study

Up to now, I have presented the various manufacturing routes that can produce UHTC polycrystalline specimens, and summarized the essential properties and characteristics of UHTCs. The potential for use of these materials in extreme environments makes the accurate determination of mechanical and physical properties

This study aims to investigate the high-temperature mechanical behavior of group IV diborides, with potential applications as composite materials in aerospace, through an ab-initio study of single crystal primitive unit cells. High temperature elasticity data is scarce for these materials systems, so this study aims to fill the voids in the literature for diborides of Zr, Hf, and Ti. This data will be used to support a pre-existing study of the microstructure of UHTCs and UHTCCs made from these materials using continuum techniques. We seek a fundamental understanding of the mechanical and thermal behavior of these UHTCCs to assess their integrity based on an optimized microstructural state.

The current study only focuses on the elastic behavior of the diborides from first princi-

ples calculations at elevated temperatures using ab-initio molecular dynamics coupled with density functional theory. The data obtained from this study is compared with Okamoto's work and other papers in the literature.

1.4.1 Outline of thesis

Chapter 1 gives a summary of the materials systems that are studied with the first-principles techniques and outlines the scope of the work. A description of the manufacturing processes and experimental limitations is provided. Chapter 2 provides a comprehensive literature review of the previous research conducted investigating the properties of these ceramic systems, from experimental work to first-principles studies. Chapters 3 and 4 focus on the theoretical foundations of the first-principles methods employed in this study and outline the important fundamental equations probed by these methods. Chapters 5 and 6 provide an overview of the methods employed and present the results of the study. Lastly, chapter 7 concludes this study with a summary of results and future work.

Chapter 2

A review of past work in ab-initio modeling of UHTCs

This chapter presents an overview of seminal works that form the basis of the current study. This includes an overview of experimental research on the group IV diborides and a look at previous work and methodologies employed by researchers in the ab-initio realm.

2.1 Research into the manufacturing of UHTCs

As described in chapter 1, the manufacturing routes of UHTCs are limited to producing small parts of fixed shape due to issues of full densification. Hot pressing routes provide avenues for full densification of the material, but limit production to very simple geometries.

The review article by Farhenholtz and Talmy [16] presents a very complete overview of the previous work in manufacturing of monolithic diborides of Zr and Hf. An overview of the manufacturing routes was provided in chapter 1, so it will not be expanded on further in this review.

2.2 Experimental studies of the mechanical behavior of group IV diborides

The mechanical properties of many of the group IV diborides were studied extensively in the past and are cataloged in monographs by Mroz [56] for ZrB_2 . As discussed in [16], many historical studies used large starting particle sizes when manufacturing the monolithic diborides that grain growth and Ostwald ripening occurred at the high sintering and densification temperatures typically chosen.

The effect of grain size on strength was studied in [79, 54] for HfB_2 based UHTCCs. In general, a Hall-Petch like behavior was observed for the strengths of these ceramics tested in three and four-point bending tests [16]. The critical grain size of anisotropic crystals of TiB_2 below which microcracking is thought not to occur was determined to be $15\text{ }\mu\text{m}$ [18]. Similar behavior is theorized to exist in ZrB_2 and HfB_2 , although values have not been established.

Elastic properties of ZrB_2 , HfB_2 and TiB_2 were studied extensively by [94]. Recent studies using a similar sonic resonance technique as the classic paper were conducted by [10] and show close agreement. Fahrenholtz [16] summarizes the elastic properties of ZrB_2 [17] and HfB_2 based ceramics and ceramic composites. Munro [57] provides a very complete listing of the material properties of TiB_2 . Polycrystalline material properties are thus very common for these materials systems.

2.2.1 Single Crystals

A landmark study was conducted by the group of Okamoto et al [63, 62] at Kyoto University where single crystals of ZrB_2 were constructed by the floating-zone process [65, 67, 66]. Otani's procedure can easily be adapted to HfB_2 and TiB_2 [65] with ease. The rectangular parallelepiped resonance method as described in [34] was used to determine the elastic constants of the single crystals of ZrB_2 . The frequency of the resonance vibrations gives the elastic constants for small parallelepipeds. Okamoto's group was also able to determine ther-

mal expansivities using a push-rod type differential dilatometry in the temperature range of room temperature to 1100°C.

Okamoto's group found that the axial elastic constants of monocrystals of TiB_2 and ZrB_2 decreased monotonically with increasing temperature. Furthermore, the transverse elastic constants (C_{12} and C_{13}) were virtually temperature independent. Okamoto also provided the bulk compressibilities and orientation dependence of Young's modulus for the various systems his group analyzed, as shown in figure 2.1.

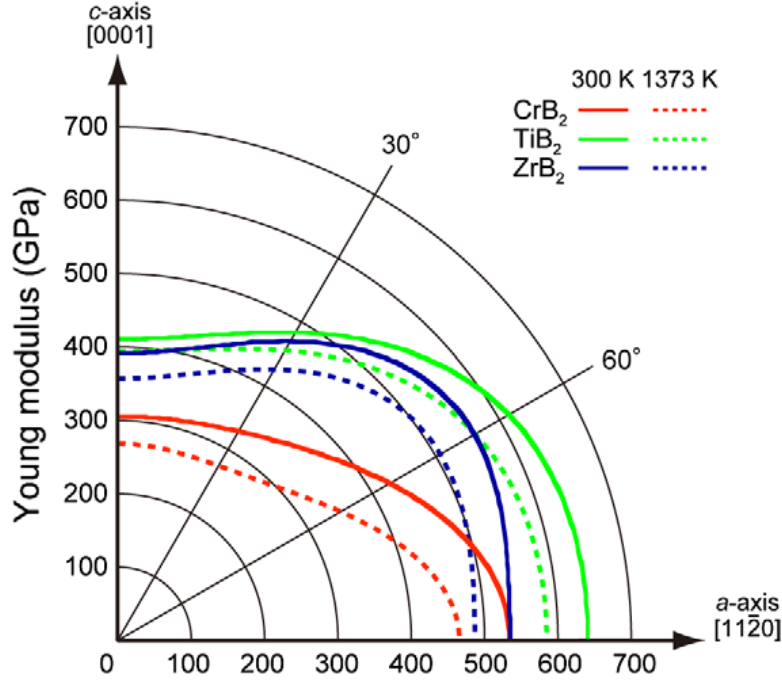


Figure 2.1: Dependence of Young's modulus on crystallographic orientation for two different temperatures for CrB_2 , TiB_2 , and ZrB_2 . Adapted from [62].

Okamoto's work motivated the current study, which analyzes the thermoelastic behavior of ZrB_2 , HfB_2 , and TiB_2 at even higher temperatures than those probed in Okamoto's work. The power of the ab-initio approach comes from the first-principles, i.e. the Schrödinger equation provides the complete behavior of any system. Atomic fluctuations from molecular dynamics simulations on primitive lattices provide a good starting point in determining the stable lattice parameter at high temperatures where, neglecting phonon interactions, the elastic constants may be determined.

2.3 Ab-initio studies

The advent of quantum calculations through the Born-Oppenheimer approximation and the use of suitable electron density functionals has propelled the study of complex many-body systems to new heights. Density functional theory and other quantum mechanical methods have become increasingly popular for analyzing systems once thought intractable. These methods have been widely used to study these ceramic systems in their ground state. However, to the author's knowledge, no high temperature elastic constants studies have been conducted. This section provides an overview of previous work in ab-initio calculations performed on these materials systems.

2.3.1 Density Functional Theory studies

The potential for ZrB_2 to be used as an epitaxial film for growth of GaN has prompted an investigation into its elastic behavior at elevated temperatures. Okamoto [63] found that there was little lattice mismatch between GaN and ZrB_2 , making it an ideal candidate for thin film growth. However, the difficulties in accessing these properties at elevated temperatures makes a theoretical study more attractive. Furthermore, Milman [45] showed discrepancy with previously determined experimental properties for TiB_2 and MgB_2 , making the experimental data come into question.

Many studies have been conducted with different pseudopotential and functional forms of DFT. A preliminary study of the ground-state elastic behavior of various AlB_2 -type structures was performed by Vajeeston et al [89]. Recent work by Mahmud and Islam [41] provides elastic constants for VB_2 and ZrB_2 using the Local Density Approximation (LDA) with the classical exchange-correlation functional of Kohn and Sham [33]. Milman [46] successfully used the plane-wave approximation using Ultrasoft pseudopotentials to study the elastic behavior of BeO. This study was able to provide ground-state elastic constants consistent with experimental theory.

Pereira et al [74] conducted a study on the behavior of different AlB_2 -type structures, including ZrB_2 using the Hartree-Fock approach with the Linear Combination of Atomic Orbitals (LCAO) as the basis for approximation. These results were compared with experimental results and were found to differ by about 10%. However, the study came into question by a recent analysis by Milman [48], which showed that the results of bulk moduli were over-estimated due to the underestimation of the cell volume. Furthermore, Milman points out that the LDA method used by Mahmud and Islam [41] will over-estimate the elastic constants and shows discrepancy with experimental data in the transverse constants to well over 10%. Refinements are still necessary to provide an accurate set of elastic constants, taking into account the shortcomings of these methods.

2.4 Recent developments

A very complete study of the ground state elastic properties of many AlB_2 structures was recently conducted by Shein and Ivanovskii [81], where they compiled the elastic constants for many single crystal MB_2 using the full-potential linearized augmented plane-wave (FP-LAPW) method with the generalized gradient approximation (GGA) for the exchange-correlation potential. Using the Voigt-Reuss-Hill models, they incorporated these single crystal values and obtained polycrystalline elastic parameters which they compared with the literature. This was the first systematic study of many of these materials systems at ground state using the FP-LAPW approach. However the high temperature properties were not explored.

Recent work by [20] provides the ground-state elastic properties of ZrB_2 as a function of pressure by employing the plane wave pseudopotential DFT with the GGA for the exchange-correlation effects. This work provided the high-temperature lattice parameters from static fluctuations at various pressures. This study, however, was not able to provide the high temperature elastic constants.

Milman [48] cites problems with the original studies of Mahmud and Islam [41] due to the

incompatible approximation of the LDA with the GGA for exchange-correlation effects. The lack of geometric optimization after applying the strain fields to the lattice breaks symmetry and thus provides deceptive results. Milman calculates the elastic constants through the finite strain approach, enforcing symmetry through a geometric optimization and close control of the self-consistent energy convergence parameters. My current work takes a very similar approach, with a couple of caveats.

2.5 The approach of this study

This study borrows from the techniques employed by Milman [48], but also incorporates the data from high temperature NPT molecular dynamics, in particular the lattice parameter fluctuations, to determine the high temperature elastic constants. The atomic fluctuations in the lattice at high temperature provide an average lattice parameter that is used to reconstruct the lattice, enforcing the same symmetry constraints as the ground state lattice. An elastic constants calculation for the “experimental” structure is then conducted, providing the possible elastic behavior at the high temperature state.

It is assumed that no solid-state phase change (either due to temperature or pressure) exists¹ and that any phonon interactions at high temperatures do not influence the elastic constants appreciably. Thus, the elastic parameters depend only on the overall expansion of the lattice at high temperatures.

Very few studies aside from the ones mentioned in this review have been conducted, most of which are still in press. None has provided the elastic constants of the diborides at high temperature, so this study hopes to fill the hole in the literature.

¹This assumption is corroborated by the literature, which shows that no known phase transformations of these materials systems in the temperature range of interest are observed

Chapter 3

Mathematical theory of the ab-initio methods: Density functional theory

This chapter explores the theory behind the ab-initio methods employed in this study. In particular, Density Functional Theory (DFT) is explored along with the theories of energy minimization and potential energy surfaces. This study analyzes the crystal structures of the group (IV) diborides with CASTEP [80], a planewave pseudopotential code written in C++. The theory behind the implementation of DFT in CASTEP is outlined along with the theory of all intermediate steps, including energy minimization and the derivation of properties from atomic fluctuations. The classical quantum chemistry approaches to solving the Schrödinger equation are discussed and a historical overview of the methods is provided.

3.1 The probabilistic nature of quantum mechanics

The discovery of the discrete energy levels of light and the wave/particle duality gave way to a revolution in the sciences.¹ The classical theories now came into question when dealing with objects of small scales. The work of Niels Bohr in dealing with discrete spectra of light

¹This discussion is based on Max Born's 1954 Nobel Lecture. Every scientist and engineer should read this lecture for an interesting historical account of how this all came to be.

and Planck's discovery of the discrete existence of energy in oscillatory processes (quanta of energy) gave rise to a new paradigm in dealing with systems of small scales. It was recognized that atomic systems could not exist in a continuum of spectra, but rather had to exist in discrete, stationary, energy states. This was the complete opposite of the classical laws which necessarily predicted a continuum of states for all classically behaving systems.

Bohr's correspondence principle was used by many scientists to great success in dealing with many new problems, as it held the promise that classical mechanics would be of close approximation to systems with high numbers of stationary states (what would later be known as principal quantum numbers). Einstein, through his work in radiation emission of light, showed that there was a transition probability that an emission, with definite frequency $\nu = (E_n - E_m)/\hbar$, would occur within a discrete energy spectra.

Heisenberg's matrix mechanics brought this period to an end, where he now considered sets of transition amplitudes of energy, rather than very definite coordinate functions of time. The ideas that non-commuting operations do not represent simultaneously observable events shocked the physics community. His philosophical principle that concepts and representations not representative of physically observable facts have no place in theoretical formulations was also adopted by Einstein when formulating his relativity theory (unknownst to him).

Together with Jordan and Heisenberg, Born published the work bringing the matrix mechanics and non-commutation of certain measurable quantities to light [7]. Simultaneously, independent work by Dirac [13] developed the same matrix mechanics without recourse to the traditional mathematical representations. However, it was Schrödinger's monumental work which now reins the supreme law of the land.

Schrödinger took the ideas from Louis de Broglie's thesis that electrons must also carry a plane wave (matter wave) with definite wavelength as a function of their momentum (thus unifying the wave-particle duality for matter), and ascribed to these waves a wave function Ψ that described their evolution with time. Thus, particles such as electrons that behave

quantum-mechanically are now considered as a continuous density distribution in space, rather than as discrete points.

Einstein's idea to treat the duality of photons and waves by considering the squared optical wave amplitude as probability density (for the occurrence of photons at a particular frequency of emission) inspired Born to assert that the new interpretation of Schrödinger's wave function Ψ be the same, i.e. $|\Psi|^2$ now represented the probability density of the electrons existing in some configuration or state Ψ [4, 5, 6].

Heisenberg would then contribute to the statistical interpretation of quantum mechanical behavior through his monumental work discovering the Uncertainty Principle [25]. The determinism of classical physics had to now be abandoned along with the consideration of atomic particles as actual material points. The definite position and velocity of an atomic particle was now not known with full confidence, thus reaffirming the probabilistic nature of quantum mechanics.

I end this historical discussion with the following, quoted verbatim from Born's Nobel lecture.²

Almost all experiments lead to statements about relative frequencies of events, even when they occur concealed under such names as effective cross section or the like.

How does it come about then, that great scientists such as Einstein, Schrödinger, and De Broglie are nevertheless dissatisfied with the situation? Of course, all these objections are levelled not against the correctness of the

²I found myself quite enamored by the historical outline in Born's Nobel Prize lecture. It made clear to me many of the spooky factors of quantum mechanics by ascribing a historical context to these ideas. I hope this short interlude helps to elucidate the underpinnings of a very fascinating, but often dogmatized subject.

formulae, but against their interpretation. Two closely knitted points of view are to be distinguished: the question of determinism and the question of reality. Newtonian mechanics is deterministic in the following sense: If the initial state (positions and velocities of all particles) of a system is accurately given, then the state at any other time (earlier or later) can be calculated from the laws of mechanics. All the other branches of classical physics have been built up according to this model. Mechanical determinism gradually became a kind of article of faith: the world as a machine, an automaton. As far as I can see, this idea has no forerunners in ancient and medieval philosophy. The idea is a product of the immense success of Newtonian mechanics, particularly in astronomy. In the 19th century it became a basic philosophical principle for the whole of exact science. I asked myself whether this was really justified. Can absolute predictions really be made for all time on the basis of the classical equations of motion?

3.2 Dirac Notation

This section provides an overview of Dirac notation, which is employed in the discussions of the Schrödinger equation. This is not intended to be a complete overview by any means. It follows the authoritative overview provided by Sakurai [78]

Consider a linear vector space \mathcal{V} that conforms to the properties of linear algebra:

$$\mathbf{v}(a + b) = \mathbf{v}(a) + \mathbf{v}(b) \quad \forall \quad \mathbf{v} \in \mathcal{V}$$

The vectors \mathbf{v} belonging to the vector space \mathcal{V} and that *span* the vector space (i.e. all vectors in that vector space may be represented as a linear combination of the vectors that *span* that space) are known as the basis vectors for that space.

Dirac's formalism develops the *bra* and *ket* vector spaces which have a dual correspondence with each other. The vector space has the dimensionality of the problem being considered (the degrees of freedom correspond to the number of alternatives or states that a particle can exist in). The *physical state* of a quantum mechanical particle or system is represented by its state vector in a complex vector space. Dirac calls this state vector its **ket**, and is denoted by:

$$|\alpha\rangle, \tag{3.1}$$

where α acts as a placeholder, “naming” the state. This ket is postulated to contain the complete information about the physical state of the system [78]. Two states can be added

$$|\alpha\rangle + |\beta\rangle = |\gamma\rangle \tag{3.2}$$

and can be multiplied by a constant:

$$c |\alpha\rangle = |\alpha\rangle c, \tag{3.3}$$

without changing its *meaning*.

A measurable observable (like position and momentum) is represented by an operator (call it A), acting on the ket from the left:

$$A \cdot (|\alpha\rangle) = A |\alpha\rangle, \tag{3.4}$$

producing another ket.

An eigenket is such that an operation produces the same ket as was operated on, differing only by a constant, known as its eigenvalue:

$$A |\alpha'\rangle = \lambda |\alpha'\rangle . \quad (3.5)$$

A ket space may be spanned by its eigenkets $|\alpha'\rangle$ ³.

By dual correspondence, to each ket $|\alpha\rangle$ there exists a corresponding bra $\langle\alpha|$. The bra space is spanned by eigenbras $\langle\alpha'|$ that are dual to the eigenkets. This dual correspondence is revealed by the complex conjugate of the ket with its constant:

$$c^* \langle\alpha| \overset{\text{D.C.}}{\longleftrightarrow} c |\alpha\rangle \quad (3.6)$$

where D.C. stands for Dual Correspondence.

The inner product now generalizes to the inner product of a complex vector space⁴. In Dirac notation, the inner product becomes:

$$\langle\beta|\alpha\rangle \quad (3.7)$$

where

$$\langle\beta|\alpha\rangle = \langle\alpha|\beta\rangle^* , \quad (3.8)$$

and

$$\langle\alpha|\alpha\rangle \geq 0, \quad (3.9)$$

the latter postulate giving the positive definite metric of the vector space.

³For a proof of this assertion, see [78].

⁴In contrast with the typical definition of inner product in real spaces as the scalar product of two vectors

From the probabilistic nature of quantum mechanics, the wavefunction can now be represented as a state ket $|\Psi\rangle$ that must fulfill conditions of orthogonality for all space:

$$\langle\Psi_i|\Psi_j\rangle=\delta_{ij} \tag{3.10}$$

$$\langle\Psi_i|\Psi_j\rangle=\int_{-\infty}^{\infty}\Psi_i^*\Psi_jd\Omega=\delta_{ij}. \tag{3.11}$$

Operators may be added by the commutative and associative axioms of algebra. Operators act on bras from the right, and kets from the left, producing another bra or ket. In general, these bras and kets are not dual to each other. The dual correspondence is given by the Hermitian adjoint of operator A , defined by:

$$A|\alpha\rangle\overset{\text{D.C.}}{\leftrightarrow}\langle\alpha|A^\dagger. \tag{3.12}$$

An operator is said to be Hermitian if:

$$A=A^\dagger. \tag{3.13}$$

All quantum mechanical operators representing real events (or measurable events) must necessarily be Hermitian. A nice proof is given in [78, 22].

3.3 The Schrödinger equation

All ab-initio studies of materials begin with the Schrödinger equation:

$$i\hbar\frac{\partial\Psi}{\partial\mathbf{x}}=-\frac{\hbar^2}{2m}\nabla^2\Psi+V\Psi, \tag{3.14}$$

where Ψ is the time-dependent wave function of the system in question. The state of the system is determined from the wave function, which can be represented in Dirac notation as

$|\Psi\rangle$. Any vector belonging to some vector space may be written in Dirac notation. Rewriting with the Dirac formalism gives:

$$i\hbar \frac{\partial |\Psi\rangle}{\partial \mathbf{x}} = -\frac{\hbar^2}{2m} \nabla^2 |\Psi\rangle + V |\Psi\rangle. \quad (3.15)$$

Defining the Hamiltonian operator:

$$\mathcal{H} = -\frac{\hbar^2}{2m} \nabla^2 + V, \quad (3.16)$$

we can rewrite the Schrödinger equation in operator form:

$$i\hbar \frac{\partial |\Psi\rangle}{\partial \mathbf{x}} = \mathcal{H} |\Psi\rangle. \quad (3.17)$$

The Schrödinger equation can be solved by separation of variables for time-independent potentials⁵. This process leads to a general solution of a superposition of time-independent eigenfunctions ψ_n with eigenvalues E_n corresponding to solutions of the time-independent Schrödinger equation:

$$\mathcal{H} |\Psi\rangle = E_n |\Psi\rangle. \quad (3.18)$$

The general solution of the time-dependent Schrödinger equation is thus a linear combination of eigenfunctions (stationary states):

$$|\Psi\rangle = \sum_{i=1}^{\infty} c_n \psi_n e^{\frac{iE_n t}{\hbar}}, \quad (3.19)$$

where c_n are constants that are used to fit the solution to any boundary condition imposed by the problem. The stationary states (i.e. solutions to the time-independent Schrödinger equation) are orthogonal:

⁵Time-dependent potentials are dealt with in the so-called Heisenberg picture. The Schrödinger picture deals with time-dependent wave functions and time-independent Hamiltonian operators. See [78, 70] for more details.

$$\langle \psi_m | \psi_n \rangle = \delta_{mn}, \quad (3.20)$$

where δ_{mn} is the Kronecker delta.

On its own, the Schrödinger equation provides eigenfunctions Ψ that do not mean much. It was the statistical interpretation of Born [4, 5, 6] that gave way to a useful meaning of the wave function. Now, the square of the wave function $|\Psi|^2$ represented the probability density that a particle would be found in the eigenstate $|\Psi\rangle$, where the eigenstate represented a particular physical state that a measurement of an observable property would represent.

3.4 The tractability of quantum mechanics

Dirac [14] mentioned in 1929 that quantum mechanics was in essence a solved problem. Progress in the study of quantum mechanical systems, because of the intractability of the Schrödinger equation for the many-body problem, necessarily depends on the development of tractable approximation techniques. Currently, Density Functional Theory has become a very popular technique among researchers in condensed matter physics to analyze many-body problems from the solution of the Schrödinger equation. The accepted way of attacking the many-body problem is by the Born-Oppenheimer approximation, which treats the electronic and nuclear motions separately [87].

3.4.1 The Born-Oppenheimer Approximation

The nuclei of atoms is roughly 1800 times more massive than the mass of the individual orbiting electrons. Thus, electrons respond much more quickly to changes in the surroundings than the nuclei do [82]. Thus, the behavior of the nuclei and of the electrons may be decoupled by invoking the Born-Oppenheimer approximation [8].

The nuclei in a set of atoms are fixed in position and the equations of motion for the electrons are solved as if they were under the influence of a fixed potential field (The Coulombic

potential of fixed nuclei). Thus, the neighboring nuclei-nuclei interactions are not taken into account, vastly simplifying the system in question.

The positions of the nuclei are fixed and are usually taken as their ground state positions. The electronic Schrödinger equation is then solved for the electronic wave function. The nuclear positions are then varied and the wavefunctions are again obtained (mind you that a numerical approximation is necessary here). By varying the positions of the nuclei, a potential energy surface (PES) is generated which describes the Hamiltonian of the energy eigenfunction.

The lowest energy configuration of the interacting electrons with the fixed nuclei is, in theory, the true state of the system⁶. Thus, by finding the lowest energy configuration of a set of electrons under the influence of a potential energy field generated by static nuclei, we are indeed finding a potential energy surface where we must find local minima to ensure that we have correctly classified the state of the system. That is a mouthful, so to recapitulate:

- The nuclei are vastly more massive than the electrons and thus the time scales where the nuclei can react to a change in the surroundings is much greater than the time that it takes the electrons to react. Thus the motions of the electrons are essentially decoupled from the motions of the nuclei.
- The nuclei are fixed in space and the equations of motion (the time independent Schrödinger equation) are solved for the electron motion separate from the nuclear motion. The electron motion only depends on the position of the nuclei and not on the momentum.
- The electrons behave as if they were under the influence of a static potential field (due to the static nuclei). The electrons thus become an inhomogeneous electron gas under the influence of an external static potential field.
- The electrons relax to instantaneous ground state more rapidly than do the nuclei.

⁶This is based on statistical thermodynamics, i.e. the classic ground state.

The electronic wavefunction is obtained with the nuclear positions as parameters. The energy of the system is then used to solve the nuclear motion problem.

By the Born-Oppenheimer approximation, the total wavefunction may be represented by an *ansatz*

$$\Psi = \Psi_e \Psi_N, \quad (3.21)$$

where Ψ_e represents the electronic wavefunction and Ψ_N represents the nuclear wavefunction. The electronic motion is thus decoupled from the nuclear motion and the Schrödinger equation may be solved for the interaction between fixed nuclei (thus creating a sort of potential field) and electrons.

The Born-Oppenheimer approximation is integral to the development of numerical methods for solving the Schrödinger equation for many-body configurations. If the nuclear motion were taken into account, the equations would form a coupled system where the interactions between nuclei and electrons were mutually dependent on each other, yielding an infinitely complex system.

3.4.2 The modified Schrödinger equation

The Hamiltonian of the system of interacting protons and electrons is given by:

$$\mathcal{H} = \underbrace{\sum_I \frac{P_I^2}{2M_I}}_{T_N} + \underbrace{\sum_i \frac{p_i^2}{2m_i}}_{T_e} + \underbrace{\sum_{i>j} \frac{e^2}{|r_i - r_j|}}_{V_{ee}} + \underbrace{\sum_{I>J} \frac{Z_I Z_J e^2}{|R_I - R_J|}}_{V_{NN}} - \underbrace{\sum_{i,I} \frac{Z_I e^2}{|R_I - r_i|}}_{V_{eN}}, \quad (3.22)$$

where we can recognize kinetic and potential energy terms. Rewriting the Hamiltonian gives:

$$T_N + T_e + V_{ee}(\mathbf{r}) + V_{NN}(\mathbf{R}) + V_{eN}(\mathbf{r}, \mathbf{R}), \quad (3.23)$$

where \mathbf{R} represents the positions of the nuclei in the system.

The electronic wavefunction Ψ_e must satisfy the time-independent Schrödinger equation incorporating the interaction between electrons and a static array of nuclei:

$$\left[-\sum_i \frac{\hbar^2}{2m_i} \nabla_i^2 - \sum_i \sum_{\alpha} \frac{Z_{\alpha}}{|r_i - r_{\alpha}|} + \frac{1}{2} \sum_i \sum_{j \neq i} \frac{1}{|r_i - r_j|} \right] \Psi_e = E_e \Psi_e, \quad (3.24)$$

where now the interaction potential terms are included and the energy eigenvalues E_e depend on the nuclear positions. The α subscript denotes the positions of the nuclei, and are parameters in the formulation. Thus, only the electronic positions are solved for with this modified Schrödinger equation.

The energy eigenvalues E_e are the adiabatic contribution of the electrons to the total energy of the system. All non-adiabatic terms are neglected on grounds that they contribute little to the total energy⁷. The nuclear wavefunction Ψ_N is thus obtained by incorporation of this adiabatic contribution to a nuclear Hamiltonian[24]:

$$\mathcal{H}_N = -\sum_{\beta} \frac{\hbar^2}{2M_{\beta}} \nabla_{\beta}^2 + E_e + \frac{1}{2} \sum_i \sum_{\gamma \neq \beta} \frac{Z_{\beta} Z_{\gamma}}{|r_{\beta} - r_{\gamma}|}, \quad (3.25)$$

and the new eigenvalue problem is solved for the nuclear energies and wavefunction:

$$\mathcal{H}_N \Psi_N = E_N \Psi_N. \quad (3.26)$$

3.5 The seminal works of Hartree, Hohenberg, and Kohn

The many-body Schrödinger equation is intractable and will only yield to mathematical approximations and numerical techniques. The Born-Oppenheimer approximation gives a good starting point for attacking such a problem.

⁷Proved using time-dependent perturbation theory. See [24] for a nice proof

The work of Hartree and Fock provided the groundwork to solving the many-body equations. Many approximation schemes would follow, including Density Functional Theory through the monumental discovery of stationary energy from a functional of electron density by Hohenberg and Kohn. This section briefly describes the chief principles of the Hartree-Fock method and the discovery of Hohenberg and Kohn, leading to the postulates of DFT.

3.5.1 Hartree-Fock Theory

The Hartree-Fock approach assumes that an N-fermion body wave function is approximated by a single Slater determinant. The variational principles of calculus are invoked to derive a set of N-coupled differential equations for the N-spin orbitals describing the wave function.

The crux of the method is a Born-Oppenheimer type ansatz, where the many-body wavefunction is composed of a product of spin orbitals⁸:

$$\Psi(\mathbf{x}_1, \mathbf{x}_2, \dots, \mathbf{x}_N) = \chi_1(\mathbf{x}_1)\chi_2(\mathbf{x}_2) \dots \chi_N(\mathbf{x}_N), \quad (3.27)$$

where now the Hartree product has been formed. However, the inherent antisymmetric nature of fermionic wave functions does not permit such a treatment. This is corrected by a Slater determinant, which takes a linear combination of symmetric and antisymmetric wave functions of the Hartree ansatz. Let us consider the case of a two fermion wave function:

$$\Psi(\mathbf{x}_1, \mathbf{x}_2) = \chi_1(\mathbf{x}_1)\chi_2(\mathbf{x}_2). \quad (3.28)$$

The antisymmetric part is combined with the symmetric terms already embodied in the Born- Oppenheimer ansatz to yield:

$$\Psi(\mathbf{x}_1, \mathbf{x}_2) = \frac{1}{\sqrt{2}} [\chi_1(\mathbf{x}_1)\chi_2(\mathbf{x}_2) - \chi_1(\mathbf{x}_2)\chi_2(\mathbf{x}_1)]. \quad (3.29)$$

This is immediately recognized as a 2×2 determinant:

⁸Different products lead to different approximation schemes, as we will seen in what follows.

$$\begin{vmatrix} \chi_1(\mathbf{x}_1) & \chi_1(\mathbf{x}_2) \\ \chi_2(\mathbf{x}_1) & \chi_2(\mathbf{x}_2) \end{vmatrix} \quad (3.30)$$

first recognized by John C. Slater in 1929 [84], and is readily extended to an N-body system to arrive at the general Slater determinant [9]:

$$\begin{vmatrix} \chi_1(\mathbf{x}_1) & \chi_1(\mathbf{x}_2) & \cdots & \chi_1(\mathbf{x}_N) \\ \chi_2(\mathbf{x}_1) & \chi_2(\mathbf{x}_2) & \cdots & \chi_2(\mathbf{x}_N) \\ \vdots & \vdots & \ddots & \vdots \\ \chi_N(\mathbf{x}_1) & \chi_N(\mathbf{x}_2) & \cdots & \chi_N(\mathbf{x}_N) \end{vmatrix}. \quad (3.31)$$

The significance of the Slater determinant comes from the enforcement of the antisymmetric conditions of a multi-fermionic wave function through matrices. The antisymmetrization of a multi-fermionic wave function is ensured through the linear combination of symmetric and antisymmetric Hartree products, generalized as a determinant. It is easily shown that:

$$\Psi(\mathbf{x}_1, \mathbf{x}_2) = -\Psi(\mathbf{x}_2, \mathbf{x}_1), \quad (3.32)$$

through the use of the Slater determinant.

What results after imposing orthonormalization conditions on the Schrödinger equation is a set of one electron equations:

$$\mathcal{H}_{HF} = T_{total} + V_{ei} + V_H + V_x \quad (3.33)$$

$$\mathcal{H}_{HF}\psi_i = E_i\psi_i, \quad (3.34)$$

where V_x represents the exchange potential, i.e. the potential between the self-interaction of electrons with different spins, formulated to comply with the Pauli exclusion principle. The Hartree component of the potential is the electrostatic potential arising from the charge

distribution (electron density).

These equations are solved with the assumed wavefunction as a Slater determinant, thus reducing the problem to that of a set of single electron problems. The method neglects correlation of electrons (spin interaction between different electrons).

3.6 The exchange-correlation terms

Some weird interactions arise when considering the total Hamiltonian of the many-body Schrödinger equation. These interaction terms involve electron-electron interactions (correlation) and electronic terms that tend to raise the energy eigenvalues through an interaction of wave functions (exchange) for different spin states of the electrons.

The exchange-correlation terms arise from consideration of the Pauli-exclusion principle. Interacting electrons in spin-polarized states cannot both have the same spin and occupy the same point in space. There is thus a fictitious “exchange hole” around each electron with a given spin so that any electron with like spin avoids the area completely. This potential is the exchange function.

Correlation occurs through Coulombic interaction between electrons with opposite spin due to their repulsion. The overall symmetry of the system (spin or dipole) also creates an electron correlation. Thus, Hartree-Fock includes some form of correlation through the exchange term (the self-interaction of electrons with equal spin).

These terms also arise in DFT, where the same Hartree terms come out from a minimization of the total energy. These exchange-correlation terms are approximated through various techniques in DFT, thus leading to a modification of the purely variational problem to one that needs a self-consistent approximation.

3.6.1 Density Functional Theory - Approach

In DFT, the total energy of the system is assumed to be a functional of the electron density, which is given as a linear combination of orbital densities (atomic orbital). The overall formulation reduces the many-body problem of interacting electrons to that of non-interacting electrons (due to the first Hohenberg-Kohn theorem) in a static potential (due to the Born-Oppenheimer approximation). This potential includes the effects of exchange and correlation.

The electron density of an N -body system is given by the sum (integral) of normalized wavefunctions [37, 68]:

$$\rho(\vec{r}) = N \int d^3r_2 \int d^3r_3 \cdots \int d^3r_N \Psi^*(\vec{r}, \vec{r}_2, \dots, \vec{r}_N) \Psi(\vec{r}, \vec{r}_2, \dots, \vec{r}_N). \quad (3.35)$$

Kohn and Sham [33] showed that the self-consistent solution of a set of single particle Schrödinger equations for the single particle orbitals ϕ_i gives the correct electron density, where density becomes a linear combination of the orbitals ϕ_i . These equations arise from the first variational of the energy functional with orthonormality constraints. A self-consistent solution involves taking a guess for the form of the orbital ϕ_i , solving the Kohn-Sham equations for the correct orbital, and calculating the density. A density mixing between input and output densities is used to assign a new density to the problem. This loop continues until a certain metric is minimized. Details of this process are provided in section 3.7.4. The next section provides an overview of the Kohn-Sham equations and their implementation in DFT.

3.7 Density Functional Theory - Implementation

By the Hohenberg-Kohn theorems [26, 33]:

- The total energy of a non-spin-polarized system of interacting electrons in an external

potential (the nuclei) is a functional of the electron density:

$$E = E[\rho] \quad (3.36)$$

$$\rho = |\Psi|^2. \quad (3.37)$$

- The true ground state density is that which minimizes the energy functional subject to orthogonality constraints:

$$\frac{\delta E[\rho]}{\delta \rho} - \sum_{i,j} \Lambda_{ij} \langle \Psi_i | \Psi_j \rangle = 0. \quad (3.38)$$

The energy functional is usually given by the total Hamiltonian [83]:

$$\mathcal{H} = T_s[\rho] + E_{eN}[\rho] + E_{NN}[\rho] + E_H[\rho] + E_{xc}[\rho], \quad (3.39)$$

where the Hartree contribution is given by:

$$E_H[\rho] = \frac{e^2}{2} \int d^3\mathbf{r} d^3\mathbf{r}' \frac{\rho(\mathbf{r})\rho(\mathbf{r}')}{|\mathbf{r} - \mathbf{r}'|}. \quad (3.40)$$

The electron density is given as a linear combination of atomic orbital densities:

$$\rho = \sum_i |\phi_i|^2. \quad (3.41)$$

A variational formulation gives a set of equations for non-interacting particles that produces the same electron density as if the particles were fully interactive. The resulting equations are Schrödinger equations for the individual single particle wavefunctions ϕ_i :

$$\left(-\frac{\hbar^2}{2m} \nabla^2 + v_{\text{eff}}(\mathbf{r}) \right) \phi_i(\mathbf{r}) = \epsilon_i \phi_i(\mathbf{r}). \quad (3.42)$$

where v_{eff} is the effective potential that takes into account the Hartree energy and effective external potential due to static nuclei:

$$v_{\text{eff}}(\mathbf{r}) = v_{\text{ext}}(\mathbf{r}) + e^2 \int \frac{\rho(\mathbf{r}')}{|\mathbf{r} - \mathbf{r}'|} d\mathbf{r}' + \frac{\delta E_{\text{xc}}[\rho]}{\delta \rho(\mathbf{r})}. \quad (3.43)$$

The last term is the exchange correlation potential, defined by:

$$\mu_{\text{xc}}(\mathbf{r}) \equiv \frac{\delta E_{\text{xc}}[\rho]}{\delta \rho(\mathbf{r})}. \quad (3.44)$$

The orbitals are obtained from the solution of equation (3.42) and are used to construct the electron density (3.41). This density is compared with the initial density based on the construction of an assumed ϕ_i . This assumed wavefunction is usually constructed by an expansion of a basis set. If the densities do not differ appreciably based on some mixing scheme and norm, then the self-consistent iteration scheme is completed and the true ground state density and energy of the system has been obtained. The total energy is related to the Kohn-Sham eigenvalues by [68]:

$$E = \sum_i^N \epsilon_i - E_H[\rho] + E_{\text{xc}}[\rho] - \int \mu_{\text{xc}} \rho(\mathbf{r}) d\mathbf{r}. \quad (3.45)$$

DFT, in contrast with the Hartree-Fock approach of section 3.5.1 systematically maps the many-body problem with an interacting potential with that of a single-body problem without the interactions.

The difficulty arises when employing the exchange-correlation functional. The simplest approximation is the Local Density Approximation (LDA), where:

$$E_{\text{xc}}[\rho] = \frac{e^2}{2} \int d^3\mathbf{r} \rho(\mathbf{r}) \epsilon_{\text{xc}}[\rho], \quad (3.46)$$

and $\epsilon_{\text{xc}}[\rho]$ is a local function of electron density. An early approximation was given by Slater [85] to be $\epsilon_{\text{xc}}[\rho] = \rho^{1/3}$. Any approximation which reproduces a known energy for a given

uniform electron density can be used.

Another common approximation is the Generalized Gradient Approximation (GGA) incorporating the local gradient of density into the functional $\epsilon_{xc}[\rho, \nabla\rho]$. The specific functionals in common use today will be discussed in section 3.7.3.

3.7.1 Basis sets

The electron density is usually chosen as a linear combination of orbitals (the Kohn-Sham orbitals). The choice of these orbitals is made to reduce computational costs [83]. The Kohn-Sham equations 3.42 are usually solved by resorting to a basis set expansion of the Kohn-Sham orbitals, the common of which is the Linear Combination of Atomic Orbitals (LCAO):

$$\phi_i = \sum_j c_{ij} \chi_j, \quad (3.47)$$

where χ_j are the atomic orbitals of the atoms in the system and c_{ij} are expansion coefficients. Other basis sets are common, depending on the application.

Periodic systems, such as crystal lattices with large seas of electrons (inhomogeneous electron gases) are commonly expanded with planewaves. By Bloch's theorem [32], the crystal momentum vector \mathbf{k} represents a conserved quantum number and gives boundary conditions for periodic wavefunctions:

$$\phi_k(\mathbf{r} + \mathbf{R}_L) = e^{i\mathbf{k} \cdot \mathbf{R}_L} \phi_k(\mathbf{r}) \quad (3.48)$$

where \mathbf{R}_L is the lattice vector. The general solution that satisfies this boundary condition is a plane wave in reciprocal space:

$$\phi_k(\mathbf{r}) = e^{i\mathbf{k} \cdot \mathbf{r}} \sum_{\mathbf{G}} c_{\mathbf{G}}(\mathbf{k}) e^{i\mathbf{G} \cdot \mathbf{r}} \quad (3.49)$$

where \mathbf{G} are the reciprocal lattice vectors for the first Brillouin zone.

A superposition of plane waves with the wavevector \mathbf{k} representing the crystal momentum provides the basis for the orbital approximation. Along with the pseudopotential approximation, the basis functions may be formulated to accurately depict electron behavior while maximizing computational efficiency.

The lattice is discretized with a k-point sampling [51] of the Brillouin zone and is expanded by plane waves at each k-point. The expansion coefficients on plane waves with small kinetic energies and larger kinetic energies are neglected (influences from far-away atoms). A cutoff energy will define the limit of accepted plane wave basis functions.

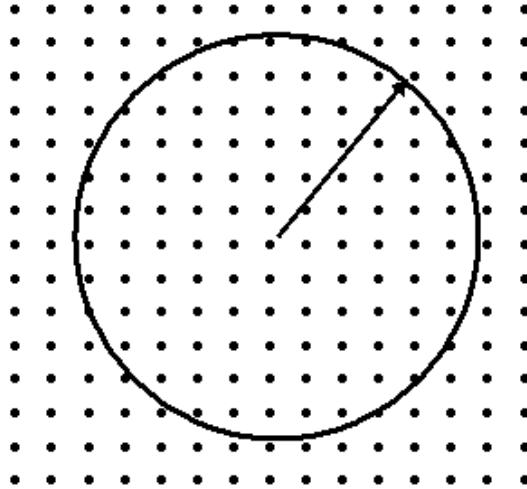


Figure 3.1: Plane waves representing energy levels beyond a certain cutoff are neglected. The radius of the sphere is proportional to the cutoff energy set during preprocessing. Adapted from [1]

Thus, a potentially infinite basis set is truncated at a finite cutoff energy set by the user (and approximately calculated by CASTEP). The k-point set and cutoff energy will define the number of basis functions based on neglecting higher energy basis functions. As the unit cell changes in size or shape, discontinuities may propagate in the basis set. A correction factor may be applied that accounts for the difference between the number of states in the basis set with an infinitely refined k-point sampling and the number of basis states actually

used [19].

To evaluate the correction term, determine the change in total energy with respect to the logarithm of the cutoff energy. If this value is less than 0.01 eV/atom, then the calculation is said to be very well converged (the basis set converged to the cutoff energy) :

$$\frac{dE}{d \ln E_{cutoff}} < 0.01 \text{eV/atom.} \quad (3.50)$$

3.7.2 Pseudopotentials

By the Fermi liquid theory (FLT), electronic excitations near the Fermi energy behave as if they were independent particles. These particles are non-interacting at low energies [83]. Core electrons bonded with nuclei have very strong interactions and do not respond to motions of the valence electrons. Thus, these electrons may be regarded as fixed.

All potentials contributing to core-nuclei interactions are not modeled exactly in the pseudopotential approach. Rather, these potentials are replaced by a single pseudopotential that has a ground state wavefunction that is essentially like the valence wavefunction [83]. This smooths out the potential energy surface and makes computations much easier. The effects of the tight core electrons with the nuclei are smoothed out so that a smaller cut-off energy is required to model the orbitals correctly (smaller basis set) [24].

The pseudopotentials employed in this study are those of Vanderbilt [91, 35, 36]: the Ultrasoft pseudopotentials. The wavefunctions in this pseudopotential approach are required to mimic the valence wavefunction outside a critical radius r_c as previously mentioned. However, within the critical radius, they can be as “soft” as possible [83]. The charge density, as a consequence, must now be written with an augmentation term. Specifics of this procedure are relegated to the original papers and to [83]. Suffice it to say, the use of these pseudopotentials greatly reduces computation time for large scale calculations by smoothing out the effects of orthonormality near the nuclei.

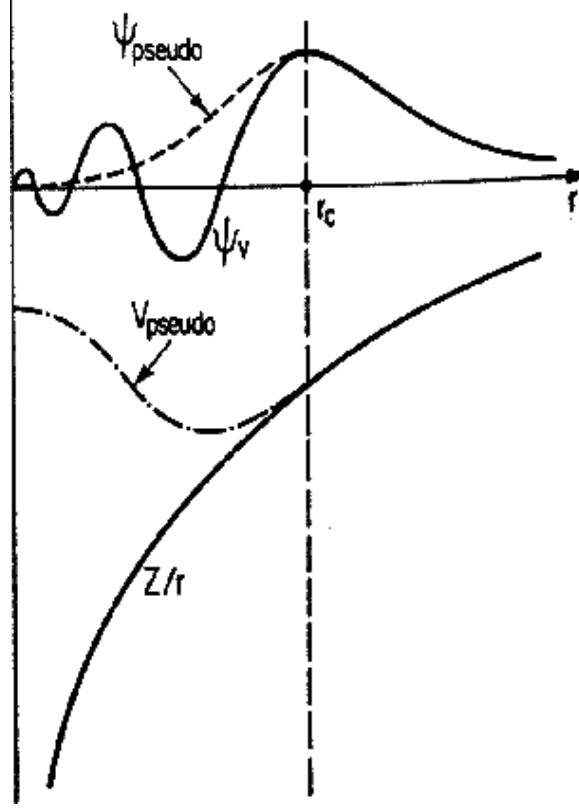


Figure 3.2: Schematic of the reformulation of the potential and wavefunction with a smoother pseudopotential. Adapted from [71]

3.7.3 Exchange and correlation functionals

The use of approximating functionals on the exchange-correlation terms destroys the variational property of the total energy. As a result, the minimum energy may not correspond to the true minimum in the rigorous sense. Rather, the new minimization process gives a very close approximation.

The LDA has found success in modeling complex ceramic systems [41]. However the GGA has shown better convergence properties and accuracy by including local gradient effects in the exchange-correlation approximation.

The functional employed in this study is that of Perdew, Burke, and Ernzerhof [72], which is an improvement over the non-local Perdew-Wang functional [73]. The exchange-correlation energy now is a functional of the electron density incorporating different spin orientations. The functional incorporates the uniform electron gas energy from the Thomas-Fermi model

and a spin-polarized enhancement factor satisfying the Lieb-Oxford bound [72]

$$\epsilon_{xc}^{\text{unif}} = \frac{-3e^2 k_F}{4\pi}, \quad (3.51)$$

where k_F is the Fermi wavenumber. The enhancement factor is defined as:

$$F_X(s) = 1 + \kappa - \kappa/(1 + \mu s^2/\kappa), \quad (3.52)$$

where $\mu = \beta(\pi^2/3)$ and $\beta \approx 0.066725$. The factor s is a density gradient:

$$s = \frac{\nabla \rho}{2k_F \rho}. \quad (3.53)$$

3.7.4 Self-consistent field calculations

With a basis for approximation, the electron density is computed from (3.41) and is used to compute the Kohn-Sham potential. Approximations made to the exchange-correlation term destroy the variational property of the energy functional. Thus, energy minimization will not necessarily provide the true ground state energy, but an over(under)-estimation depending on the formulation for the exchange-correlation potential [83].

Incorporating the Kohn-Sham potential (equation (3.43)) into the Kohn-Sham equations and taking the first variational leads to a variation of the expansion parameters c_{ij} . Thus, the solution of (3.42) depends on finding the parameters c_{ij} that minimize the energy. The determination of the coefficients is separated from the calculation of the self-consistent electron density, where the coefficients are repeatedly determined that solve the equations (3.42) for a fixed charge density.

Substituting equation (3.47) into (3.42) gives the following matrix form⁹:

$$\mathbf{HC} = \epsilon \mathbf{SC} \quad (3.54)$$

⁹See Sakurai [78] for the definition of matrix elements from bra-ket formalism

where

$$H_{ij} = \left\langle \chi_i(\mathbf{r}) \left| \frac{-\hbar^2}{2m} \nabla^2 - V_{NN} + V_{ee} + \mu_{xc} \rho(\mathbf{r}) \right| \chi_j(\mathbf{r}) \right\rangle, \quad (3.55)$$

and

$$S_{ij} = \langle \chi_i(\mathbf{r}) | \chi_j(\mathbf{r}) \rangle. \quad (3.56)$$

This eigenvalue problem is solved with conventional matrix techniques for the matrix \mathbf{C} , which has the coefficients of the basis expansion.

The self-consistent iterative procedure can thus be outlined as follows [1]:

- Choose an initial set of constants to populate matrix \mathbf{C} .
- Construct the initial set of molecular orbitals (wavefunctions) ϕ_i .
- Construct the electron density from (3.41).
- Construct the Kohn-Sham potential (3.43).
- Construct matrix \mathbf{H} .
- Solve the matrix eigenvalue problem (3.54) for a new matrix \mathbf{C} .
- Construct new molecular orbitals and electron density.
- Perform adequate electron density mixing (straight, Pulay, etc.¹⁰)
- If the density is minimum by comparison with the original density (i.e. if the normed distance between densities is minimum based on a residual), then solve for the ground state energy by equation (3.45). This energy now becomes the new ground state.

Repeat the procedure if the minimum has not been found.

¹⁰See section 3.7.5 for more details

The self-consistent field procedure outlined above is the core of the Kohn-Sham formalism along with the Kohn-Sham equations. The solutions to the modified Schrödinger equations now involve guessing a wavefunction with a basis expansion, solving for the variable coefficients of the basis expansion, and rebuilding the basis with new coefficients until the difference between the electron densities is minimum.

In essence, this is another way of solving the many-body PDE arising from the Schrödinger equation with a basis approximation, employing an iterative scheme to minimize the residual that makes the energy minimum. Conventional numerical integration is used for the exchange-correlation potential μ_{xc} in the Kohn-Sham potential.

3.7.5 Density Mixing

The self-consistent iteration scheme takes the calculated density and mixes it with the original input to yield a refined guess and improve stability of the numerical method [83]. The simplest form is straight mixing:

$$\rho_{in}^{i+1} = (1 - \alpha)\rho_{in}^i + \alpha\rho_{out}^i, \quad (3.57)$$

where α is a mixing parameter, depending on the tradeoff between convergence rate and radius of convergence [83].

This study employs Pulay mixing [76], which was first conceived to improve convergence in the SCF iterations in Hartree-Fock methods. The approach essentially involves constructing a linear combination of error vectors (differences in densities) from previous iterations and uses these vectors in a least-squares fit of the null vector. The coefficients of the least-squares fit are used to extrapolate the new density from the difference in calculated density (the error)!¹¹

¹¹I found this method to be very ingenious. Please see [76] for a greater appreciation of the method.

3.8 Summary

This chapter dealt with the theoretical underpinnings of the common ab-initio methods used to study molecular systems. We are now poised to explore the ab-initio molecular dynamics methods that are coupled with DFT to explore atomistic systems at their electronic level at high temperatures. The trajectories of the lattices will provide the data needed to extract the elastic properties of the material, along with many important physical and mechanical properties.

The next chapter provides a theoretical overview of molecular dynamics applied to ab-initio systems. These methods are used in this study to probe the high temperature structures of the complex diboride systems mentioned in chapter 1 and extract the mechanical behavior.

Chapter 4

Ab-initio molecular dynamics and its application to the group IV diborides

The analysis of complex ceramic systems at high temperatures requires the integration of DFT with molecular dynamics so that trajectories can produce the average static and dynamic properties of interest. What results is the ab-initio molecular dynamics approach, which is consistent with classical molecular dynamics.

This chapter gives a brief overview of the ab-initio molecular dynamics method, recalling some basic factors from the classical method.¹

4.1 Classical Lagrangian and Hamiltonian dynamics

Classically, the dynamics of interacting particles and multi-body systems can be condensed to a variational re-statement of the Newtonian equations of motion. The variational approach yields the Euler-Lagrange equations for conservative systems:

$$\frac{d}{dt} \frac{\partial L}{\partial \dot{x}_i} - \frac{\partial L}{\partial x_i} = 0, \quad (4.1)$$

¹The treatment of the ab-initio MD approach follows that of Marx [43] and isn't nearly as exhaustive. Only the most important factors of the method will be discussed, keeping this chapter as brief as possible

which can be used in conjunction with constraints to yield the differential equations governing the motion of the system. This was a dramatic improvement to the deterministic Newtonian equations, which analyzed the position of every material particle under the influence of external forces [21]. The Lagrangian L is a representation of the difference between kinetic and potential energies of a system.

In Hamiltonian dynamics, a functional of position and momentum is defined that is invariant under time transformation [23]. This functional is the Hamiltonian, and represents the total energy of the system (consistent with the first law of thermodynamics):

$$\mathcal{H}(\mathbf{r}, \mathbf{p}) = \text{const.} \quad (4.2)$$

The Hamiltonian for an N-particle system is denoted by:

$$\mathcal{H}(\mathbf{r}, \mathbf{p}) = \frac{1}{2m} \sum_i \mathbf{p}_i^2 + V(\mathbf{r}) = E, \quad (4.3)$$

and must be invariant for isolated systems under time change²:

$$\frac{d\mathcal{H}(\mathbf{r}, \mathbf{p})}{dt} = \frac{1}{m} \sum_i \mathbf{p}_i \cdot \dot{\mathbf{p}}_i + \sum_i \frac{\partial V(\mathbf{r})}{\partial \mathbf{r}_i} \cdot \dot{\mathbf{r}}_i = 0. \quad (4.4)$$

This, on comparing with the definition of the total time derivative, gives the Hamiltonian equations of motion:

$$\frac{\partial \mathcal{H}(\mathbf{r})}{\partial \mathbf{p}_i} = \frac{\mathbf{p}_i}{m} = \dot{\mathbf{r}}_i \quad (4.5)$$

$$\frac{\partial \mathcal{H}(\mathbf{r})}{\partial \mathbf{r}_i} = -\dot{\mathbf{p}}_i. \quad (4.6)$$

Combining with the Newtonian equations of motion gives the relationship for the forces on

²In the classical Schrödinger picture, the Hamiltonian is not permitted to vary with time. The wavefunction evolves with time based on the Schrödinger equation. The Heisenberg picture provides equations where the Hamiltonian (but not the wavefunction) can vary with time

the particles:

$$\mathbf{F}_i = -\frac{\partial V}{\partial \mathbf{r}_i}. \quad (4.7)$$

4.2 Classical Molecular Dynamics

In MD, the Hamiltonian equations of motion are integrated in time based on a potential function governing the behavior of the atoms and the forces on the particles are obtained³. The accelerations are determined and subsequently the positions and velocities are obtained by a suitable differencing algorithm (Velocity Verlet).

The potentials describing the interactions of the particles are known a priori in classical MD. These potentials may be empirically fitted, semi-empirically derived (Matrix mechanics), or even be hybridly related to quantum mechanical potentials (coarse graining to determine force field). Because of the Born-Oppenheimer approximation, the electrons in atoms essentially behave as if they were subjected to a stationary potential energy surface. Thus, there is a stationary external potential in addition to the interacting terms in the valence electrons of the atoms.

Particles are treated as spheres (hard or soft, depending on potential) that interact with each other over a critical radius of interaction. If a particle is within the critical radius of the particle under analysis, there will be an interaction contributing to the potential (i.e. force) of the particle.

Due to the conservative nature of the energy (Hamiltonian) function, any fluctuations produced in an isolated system must fluctuate about a constant energy. By the ergodic hypothesis [23], the ensemble average of the energies of each particle in the system is equal to the time average of the total energy of the system. For a constant of motion like the Hamiltonian, any MD simulation should show an average fluctuation about a constant energy, equal to the kinetic energy by the equipartition principle:

³All forces are considered derivable from a potential, as atomistic systems are conservative in nature

$$\langle E_k \rangle = \lim_{t \rightarrow 0} \frac{1}{t} \int_{t_0}^t E_k(\mathbf{p}) d\tau = \frac{3}{2} N k_B T. \quad (4.8)$$

4.2.1 Deriving Properties

Macroscopic properties depend on the ergodic hypothesis in classical molecular dynamics. Ensemble averages of particle trajectories (i.e. the time evolution of position and momentum) provide the properties based on statistical mechanics formulations. Thermodynamic response functions are related to the total energy (i.e. the internal energy) of the system. If the energy is known from the particle trajectories, then the differential change can provide the isometric heat capacity:

$$C_v = \left(\frac{\partial E}{\partial T} \right)_V. \quad (4.9)$$

The mean-squared fluctuations of energy usually provide the values of the analytical derivatives for these properties. The elastic constants are related to the potential energy surface of a material⁴ and can be determined from the total energy by:

$$C_{ij} = \left(\frac{\partial E}{\partial \epsilon_{ij}} \right)_P, \quad (4.10)$$

where ϵ_{ij} is the small strain tensor. An MD simulation can provide the trajectory (positions and velocities) of atoms in a lattice at different test conditions. Coupled with DFT to determine energy, the elastic behavior can be determined simply by applying a strain on a lattice and observing the energy changes! Many other thermodynamic and physical properties are derivable from atomic fluctuations based on the ergodic hypothesis.

⁴Due to the assumed linear relationship from Hooke's law and further refinements by Cauchy and Poisson

4.3 The Ab-initio Formulation

Usually called “on-the-fly” molecular dynamics because of the way the forces are computed, the ab-initio approach incorporates the effects of electron interactions to determine a more precise potential energy surface. The trajectory constantly evolves, leading to a statistical representation of the behavior of the atomic system.

This section focuses on the Born-Oppenheimer implementation of the ab-initio MD technique. The different statistical ensembles are described, and an overview of the different thermostating and barostating methods is provided.

4.3.1 Born-Oppenheimer Dynamics

Beginning from the Born-Oppenheimer approximation, an electronic form of the Schrödinger equation is obtained (3.24). From the Born-Oppenheimer approximation (3.21), the nuclear and electronic motions become decoupled and the nuclear motions are determined from the energy eigenvalues of the electronic state.

The nuclei are now approximated as classical point particles [43] by rewriting the nuclear wavefunction derived from the eigenvalue equation using a nuclear Hamiltonian (3.25). However, it is the ensemble average of the electronic Hamiltonian that provides the forces on each nuclei. These nuclei now evolve based on the nuclear Hamiltonian and the Schrödinger equation.

The electronic Hamiltonian necessarily depends on some electronic structure method such as Hartree-Fock, or in the case of CASTEP, DFT.

Specifics

Given the static potential from the fixed nuclei, the electronic structure problem (The electronic Schrödinger equation) is solved at each molecular dynamics time step. The motions of the nuclei are then created by regarding them as classical point particles and solving the

Hamiltonian equations of motion.

Each step in the time integration of the equations of motion must follow the minimization of the electronic Hamiltonian expectation value. This results in the following method [43]:

$$M_I \ddot{\mathbf{R}}_I = -\nabla_I \min_{\Psi_0} \{ \langle \Psi_0 | \mathcal{H}_e | \Psi_0 \rangle \} \quad (4.11)$$

$$E_0 \Psi_0 = \mathcal{H}_e \Psi_0. \quad (4.12)$$

The nuclear equation of motion now becomes a classical dynamics equation, with the ensemble average of the electronic Hamiltonian acting as the potential term. The wavefunctions are determined by solution of the electronic Schrödinger equation (The Kohn-Sham equations).

Minimization of the electronic Hamiltonian must be conducted at each time step to ensure that the particles are still on the Born-Oppenheimer surface. Thus, the interaction potential has the same meaning as the Kohn-Sham energy. A Lagrangian may be derived for the Born-Oppenheimer dynamics by:

$$L_{BO} = \sum_{I=1}^N \frac{1}{2} M_I \dot{\mathbf{R}}_I^2 - \min_{\phi_i} \mathcal{H}_e, \quad (4.13)$$

which after substituting into the Euler-Lagrange equations and applying orthogonality constraints via Lagrange multipliers leads to equations (4.12).

4.3.2 Ensembles

The different statistical ensembles provide control over the changing properties of the system. From the microcanonical ensemble that does not permit change in energy, size, or number of molecules in the system, to the more advanced ensembles where pressure and temperature are controlled, these ensembles provide close simulation of real molecular events under controlled conditions.

The microcanonical ensemble (NVE) allows for exploration of the constant potential energy surface (PES) without introducing the perturbations of temperature and pressure control. It provides a good test simulation to gage the parameters used for temperature and pressure control, in case there is a drift in energy.

The canonical ensemble (NVT) now simulates the structure at a controlled temperature without being coupled with a pressure bath, thus providing less perturbation in the trajectory [1]. Conformational searches may be conducting in vacuum with this ensemble. Temperature is usually controlled by a thermostat that can reproduce the ensemble conditions (i.e. truly isothermal). Temperature scaling may be used to initialize temperatures. The chain of Nosé-Hoover thermostats (section 4.3.3) is the preferred method to control the temperature.

For simulation of a lattice at an elevated (controlled) temperature and pressure, the NPT ensemble gives an appropriate simulation of the conditions. The number of molecules remains fixed (isolated system) and the pressure and temperature are controlled by contact with some some kind of external (fictitious) heat bath. The atoms are allowed to fluctuate and so a lattice of atoms is allowed to change size to incorporate pressure control. The Parrinello-Rahman barostat [69] provides pressure control by allowing the cell to change shape as well as size, thus providing a way to investigate phase transitions under pressure.

The dynamics of these different ensembles is governed by the Hamiltonian for the system. Table 4.1 shows the different ensembles used to simulate the dynamics of particles. Each ensemble offers different control over the lattice and different output properties depending on the control variables. The reader is encouraged to do a thorough investigation of the requirements of the analysis before choosing an ensemble.

4.3.3 Temperature and Pressure Control

The NVT, NPH, and NPT ensembles mentioned above require control of pressure and temperature. This is done by extending the definition of the Hamiltonian for each ensemble.

Table 4.1: A look at the different statistical ensembles.

Ensemble	Hamiltonian
NVE	$E = \langle \Psi H_e \Psi \rangle + \frac{1}{2} \sum_{i=1}^N \sum_{j=1}^N \frac{Z_i Z_j}{ \mathbf{R}_i - \mathbf{R}_j } + \sum_{i=1}^N \frac{p_i^2}{2M_i}$
NVT	$\mathcal{H} = \langle \Psi H_e \Psi \rangle + \frac{1}{2} \sum_{i=1}^N \sum_{j=1}^N \frac{Z_i Z_j}{ \mathbf{R}_i - \mathbf{R}_j } + \sum_{i=1}^N \frac{p_i^2}{2M_i} + \sum_{i=1}^M \frac{p_{\xi_i}^2}{2Q_i} + N_f k_B T \xi_1 + k_B T \sum_{i=2}^M \xi_i$
NPH (Andersen)	$\langle \Psi H_e \Psi \rangle + \frac{1}{2} \sum_{i=1}^N \sum_{j=1}^N \frac{Z_i Z_j}{ \mathbf{R}_i - \mathbf{R}_j } + \sum_{i=1}^N \frac{p_i^2}{2M_i} + P_{ext} V + \frac{p_e^2}{2W}$
NPH (Parrinello-Rahman)	$\langle \Psi H_e \Psi \rangle + \frac{1}{2} \sum_{i=1}^N \sum_{j=1}^N \frac{Z_i Z_j}{ \mathbf{R}_i - \mathbf{R}_j } + \sum_{i=1}^N \frac{p_i^2}{2M_i} + P_{ext} V + \frac{\text{tr}[\mathbf{P}_{\mathbf{g}} \cdot \mathbf{P}_{\mathbf{g}}^T]}{2W}$
NPT (Andersen)	$\langle \Psi H_e \Psi \rangle + \frac{1}{2} \sum_{i=1}^N \sum_{j=1}^N \frac{Z_i Z_j}{ \mathbf{R}_i - \mathbf{R}_j } + \sum_{i=1}^N \frac{p_i^2}{2M_i} + P_{ext} V + \frac{p_e^2}{2W} + \sum_{i=1}^M \frac{p_{\xi_i}^2}{2Q_i} + N_f k_B T \xi_1 + k_B T \sum_{i=2}^M \xi_i + \sum_{i=1}^M \frac{p_{\xi_{bi}}^2}{2Q_i} + k_B T \sum_{i=2}^M \xi_{bi}$
NPT (Parrinello-Rahman)	$\langle \Psi H_e \Psi \rangle + \frac{1}{2} \sum_{i=1}^N \sum_{j=1}^N \frac{Z_i Z_j}{ \mathbf{R}_i - \mathbf{R}_j } + \sum_{i=1}^N \frac{p_i^2}{2M_i} + P_{ext} V + \frac{\text{tr}[\mathbf{P}_{\mathbf{g}} \cdot \mathbf{P}_{\mathbf{g}}^T]}{2W} + \sum_{i=1}^M \frac{p_{\xi_i}^2}{2Q_i} + N_f k_B T \xi_1 + k_B T \sum_{i=2}^M \xi_i + \sum_{i=1}^M \frac{p_{\xi_{bi}}^2}{2Q_i} + 9k_B T \xi_{bi} + k_B T \sum_{i=2}^M \xi_{bi}$

Temperature

The preferred method for temperature control has become the Nosé-Hoover thermostat [61, 27, 60] modified by Martyna [42]. In the Nosé-Hoover thermostat method, the canonical ensembles are generated in both coordinate and momentum space and is truly an isothermal method. An additional degree of freedom is added to the structure, to represent the interaction of the structure with the heat bath [1]. The equations of motion with the extended Hamiltonian are now solved and if the degree of freedom is chosen correctly, the canonical ensemble is recovered.

This new Hamiltonian is described by:

$$\mathcal{H}^* = \sum_i \frac{p_i^2}{2m_i} + \phi(\mathbf{q}) + \frac{q}{2}\zeta^2 + gk_B T \ln S \quad (4.14)$$

for generalized coordinates \mathbf{q} and fictitious coordinates ζ and S . The Hamiltonian equations are now solved:

$$\frac{d\mathbf{q}_i}{dt} = \frac{\mathbf{p}_i}{m_i} \quad (4.15)$$

$$\frac{d\mathbf{p}_i}{dt} = -\frac{d\phi}{d\mathbf{q}_i} - \zeta\mathbf{p}_i \quad (4.16)$$

$$\frac{d\zeta}{dt} = \frac{\sum \frac{p_i^2}{m_i} - gk_B T}{Q} \quad (4.17)$$

where Q is defined as a function of the user defined q-ratio (defined in CASTEP) [1], g are the total degrees of freedom, and T is the temperature. The choice of Q is arbitrary, but is critical to the success of a run. CASTEP chooses Q automatically, but can be modified with a user-defined multiplier.

Pressure

In a molecular system, pressure is calculated through the Virial theorem [32]:

$$PV = Nk_B T + \frac{2}{3} \langle W \rangle \quad (4.18)$$

where W is the work done on each particle:

$$W = \frac{1}{2} \sum_{i=1}^N \mathbf{r}_i \cdot \mathbf{f}_i. \quad (4.19)$$

The method of controlling pressure should produce the correct statistical ensemble, i.e. that the probability of occurrence of a certain configuration obeys the laws of statistical mechanics [32].

This study employs the Andersen method of pressure control where the lattice is allowed to expand and contract isotropically in response to the temperature and atomic fluctuations. This is done to preserve the cell shape and cell symmetry. No observed solid-phase transition at the temperatures analyzed exist for these diborides, so it is assumed that cell shape is invariant in these simulations.

The volume of the unit cell is treated as a dynamic variable of the system. The Lagrangian is then modified so that it contains a user-defined term: a “mass” that serves to increase the relaxation time of the system, thus damping out pressure fluctuations. The cell relaxation time is the variable of interest and is chosen so that pressure is damped at a rate proportional to the lowest relaxation time of the system. This variable is treated in greater detail in the methodology section.

4.4 Conclusion

This chapter provided an abridged look at the theory behind the ab-initio molecular dynamics methods employed in this study. The molecular dynamics approach, coupled with the electronic structure DFT methods provides the behavior of the structure without recourse to semi-empirical methods or empirically derived potentials. Thus, the potential force-field

is derived “on-the-fly”, leading to a set of equations dependent on the wavefunction (the “first-principles”).

The subsequent chapters are devoted to the analysis of the single crystal diborides with these methods. The results of the ab-initio molecular dynamics calculations provided the trajectories and fluctuations necessary to calculate statistical averages for macroscopic properties.

Chapter 5

Methodology

This chapter focuses on the approach followed for analyzing the diboride systems using ab-initio MD and DFT. An outline of the parameters used for the analysis is provided, along with the methodology for selecting parameters. A look at the technique to determine the time step and thermostatting parameters is also provided.

5.1 Building the models

An initial model of the different diborides was first generated in the Materials Visualizer from Accelrys, Inc [1] based on the data from [16] and are shown in figure 5.1. The diboride single crystals belong to the $P6/mmm$ space group, with the metal atom occupying the 1a Wyckoff site and the boron atoms occupying the 2d Wyckoff site [48, 15]. These diborides have a simple closed-packed hexagonal structure with alternating metal and boron networks, as shown in figure 5.2. The atoms were spatially positioned according to the space group and bonding was automatically calculated. Each model was then cleaned accordingly and the lattice constants were compared with those of reference calculations. The initial lattice parameters used came from the literature [16, 48, 15, 50]. The initial lattice structure for TiB_2 was adapted from crystallography.net¹ and was originally constructed from the data

¹<http://www.crystallography.net/>

Table 5.1: The equilibrium lattice constants of the group IV diborides.

Diboride	a (Å)	c (Å)	c/a	Comment
ZrB ₂	3.169	3.530	1.114	Experimental [16]
HfB ₂	3.141	3.470	1.105	Experimental [16]
TiB ₂	3.029	3.228	1.066	Experimental [50]

by Moehler [50]. Table 5.1 shows a listing of the lattice parameters used for the diborides.

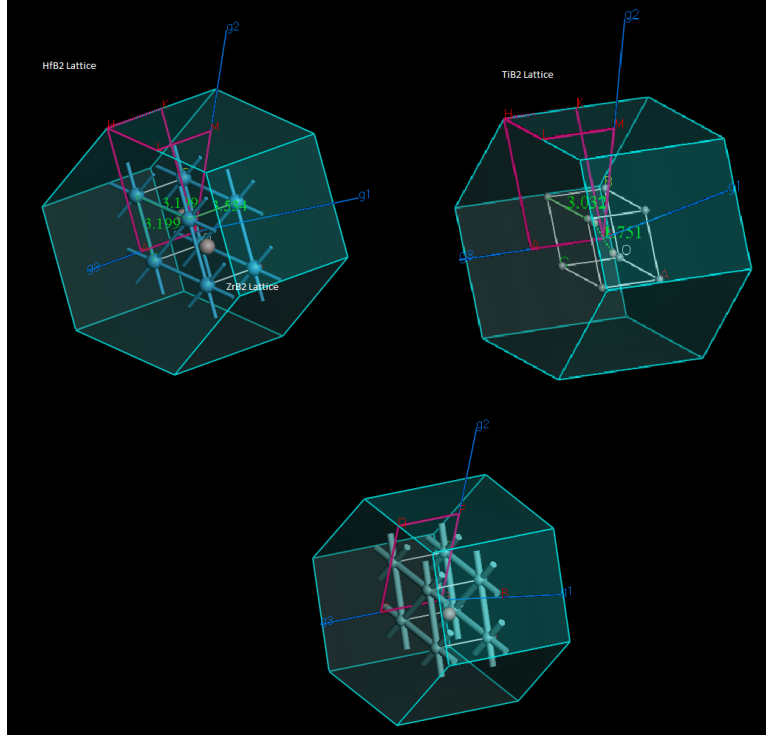


Figure 5.1: The three diboride crystals which are the focus of this study.

5.1.1 Lattice parameter refinement

After building the initial structures, a geometry optimization using the PBE version [72] of the GGA, atmospheric pressure, and the BFGS algorithm was done on each structure. Ultra-fine parameters were used, where the only default parameter modified was the maximum number of SCF cycles. A cutoff energy of 300 eV with a fine FFT grid and automatic finite basis correction was used for the basis set. An SCF tolerance of 1×10^{-6} eV/atom with the Pulay density mixing algorithm was used for the SCF residual criterion. Monkhorst-

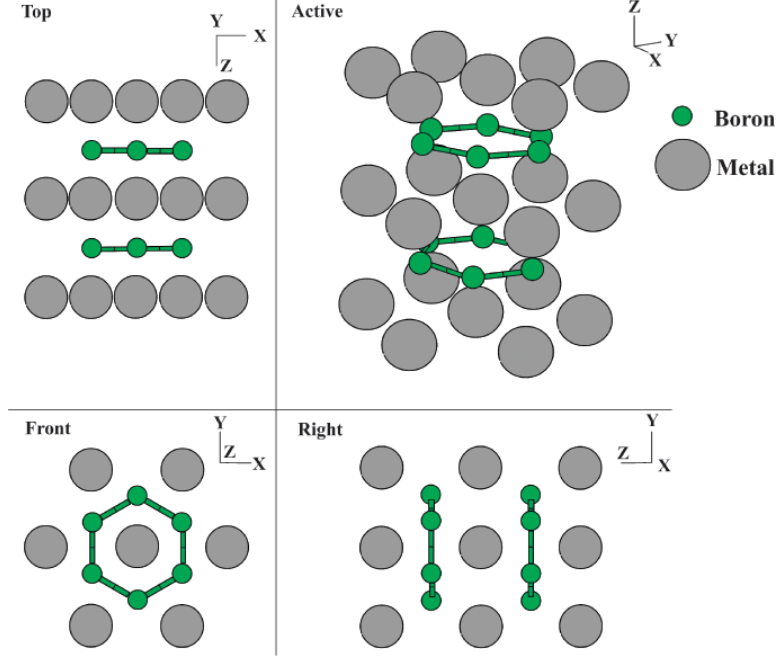


Figure 5.2: The P6/mmm space group that all diborides share. There are alternating networks of boron and metal atoms. Adapted from [16].

Table 5.2: Input parameters for initial geometry optimization.

Parameter	ZrB ₂	HfB ₂	TiB ₂
Convergence Tol.	1.0×10^{-6} eV/atom	1.0×10^{-6} eV/atom	1.0×10^{-6} eV/atom
Max. Force	0.01 eV/Å	0.01 eV/Å	0.01 eV/Å
Max. Iterations	500	1000	1000
Energy cutoff	300 eV/atom	300 eV/atom	310 eV/atom
SCF Tol.	1.0×10^{-6} eV/atom	1.0×10^{-6} eV/atom	1.0×10^{-6} eV/atom

Pack sampling with a 0.04 \AA^{-1} separation was used for the k-point discretization of the first Brillouin zone [51]. The ultrasoft pseudopotentials of Vanderbilt [91, 35, 36] were used for the modification of the potentials in reciprocal space. Similar parameters were employed for the other models, with very little difference, as summarized in table 5.2. The same parameters were implemented for the MD analysis, save for the cutoff energies, which were relaxed depending on the structure, as shown in section 5.2.

The geometry optimization refined the lattice parameters, although by only hundredths of an angstrom in some cases. The optimized structures would serve as the starting point for all high temperature simulations. The new parameters are shown in table 5.3

Table 5.3: The equilibrium lattice constants of the group IV diborides after geometry optimization.

Diboride	a (Å)	c (Å)	c/a	Comment
ZrB ₂	3.172	3.544	1.117	PBE this study
HfB ₂	3.141	3.479	1.108	PBE this study
TiB ₂	3.032	3.230	1.065	PBE this study

5.2 Initial parameter setup for MD analysis

Based on the work by Milman [48], we implemented the GGA approximation to the exchange-correlation energy for our MD calculations. The optimized structures were run in an NVE MD ensemble at different time steps at 273 K and atmospheric pressure to determine an optimal time step based on the total energy variation. The simulation showed deviation of less than ± 0.01 eV in the Hamiltonian between 0.5 and 1.0 fs simulations. A time step of 1.0 fs was chosen as a compromise between expediency and accuracy. Shorter time steps were used on some structures, namely TiB₂ to observe any plateauing effect in the constant of motion. Oscillations about a mean value were observed in these cases.

The NVE simulation also served to show the effectiveness of the thermostatting. Fluctuations were mitigated by adjusting the fictitious mass for the Nosé-Hoover thermostat. The Nosé-Hoover fictitious mass is controlled by the user-defined q ratio in CASTEP. This value was chosen as proportional to [60]:

$$q \propto gk_B T \quad (5.1)$$

where g is the number of degrees of freedom in the system, k_B is Boltzmann’s constant, and T is the simulated temperature. This proportionality constant was adjusted to 8 for a 1 fs time step based on the mitigation of fluctuations observed from the NVE study at 273 K.

The NPT ensemble was selected to simulate the elevated temperature conditions of the structure. As suggested in [48], the GGA shows good correlation for elastic constants analysis at the ground state as compared with the Local Density Approximation (LDA). A

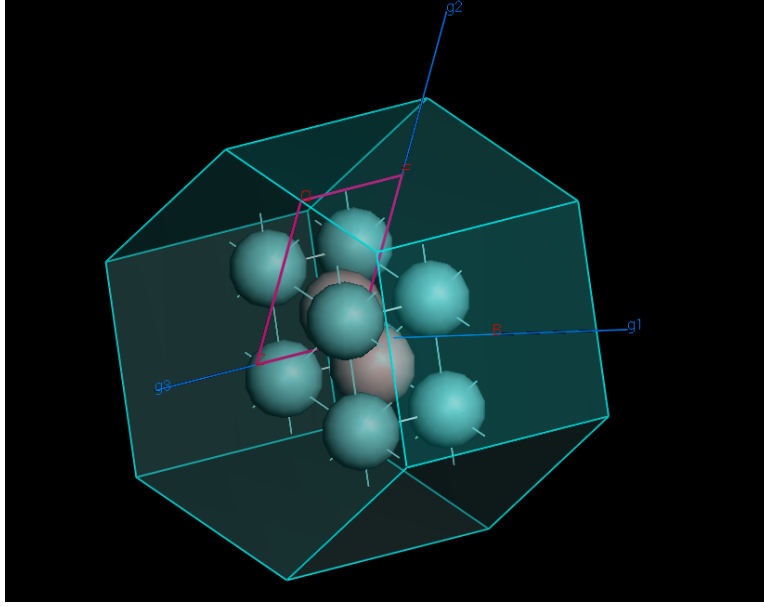


Figure 5.3: A conventional unit cell of ZrB_2 .

conventional unit cell representation as shown in figure 5.3 shows remarkable fidelity with theoretical and experimental results for many structures as shown by [48]. A basis set cut off energy of 270 eV was selected for the MD analysis for all three diborides. A chain of 5 Nose-Hoover thermostats was used for temperature control [42]. The lattice center of mass was constrained so that no cell drift was observed in the simulation. Monkhorst-Pack sampling [51] of the Brillouin Zone was employed with a k-point separation of 0.04 \AA^{-1} (A k-point mesh of $9 \times 9 \times 7$). A self-consistent field (SCF) convergence requirement of 1×10^{-6} eV was employed and the simulations converged at an average of 9 iterations during the Born-Oppenheimer minimization routines.

The Andersen-Hoover Barostat [27] was used for pressure control so that the lattice expansion was homogeneous. A cell time constant of 3.0 ps was selected based on the Nosé-Hoover fictitious mass and the control of the pressure fluctuations for the initial simulations. This factor was scaled slightly at higher temperatures based on observed fluctuations for short-time simulations.

5.3 MD simulation specifics

Based on results by Milman [48], a basic unit cell was found sufficient to model the behavior of the diborides. These results were confirmed by generating $2 \times 2 \times 2$ supercell for the HfB_2 structure and analyzing the lattice fluctuations at a single temperature.² Figure 5.4 shows the supercell structure. The results of the lattice parameter fluctuation differ slightly from the unit cell, within an acceptable range [48]. Results of the simulation are presented in the next chapter.

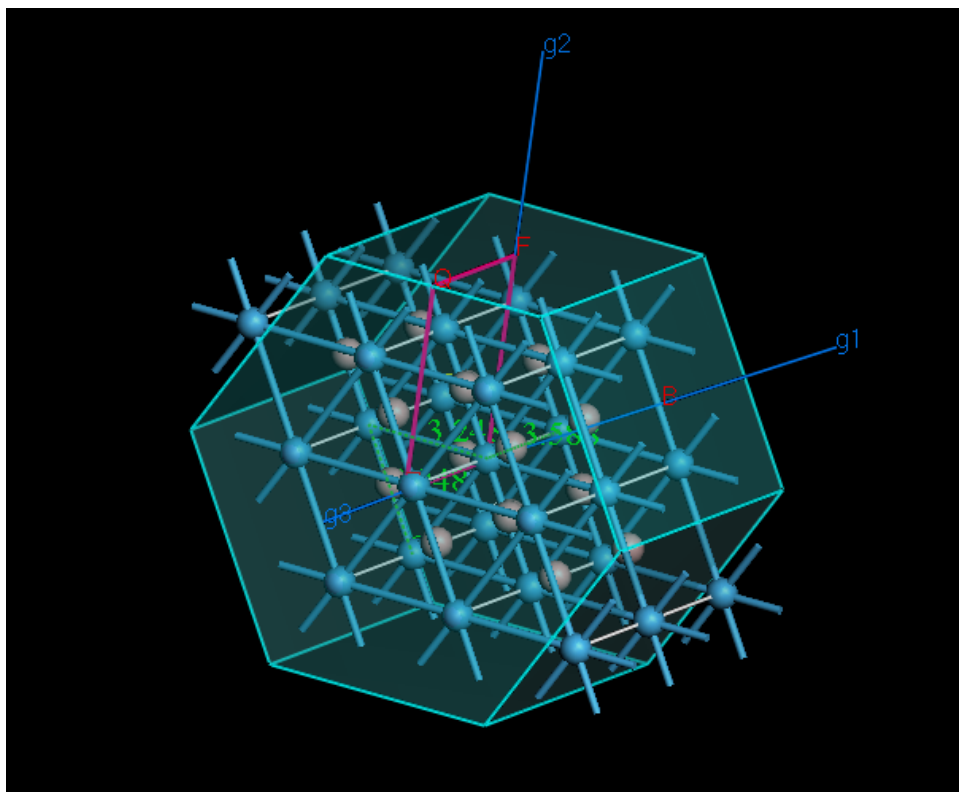


Figure 5.4: The HfB_2 supercell used to confirm the findings from Milman [48] that a single unit cell should be sufficient to track the properties of the system.

These preliminary dynamics simulations were carried out for 0.5 ps with a 1 fs time step. The results of these simulations provided a trajectory of the lattice at different temperatures. The lattice parameters were obtained by an ensemble average of the lattice vector variations during the simulation. These averages provided new lattice parameters that would be used

²Due to computational and time constraints, only a single supercell structure was analyzed

to reconstruct the lattice. It should be noted that the phonon effects are ignored and that an ensemble of these lattices should be taken to improve accuracy.

The energy fluctuations of the Born-Oppenheimer Hamiltonian and ensemble Hamiltonian were also compared to adjust parameters. There was little observed drift in the constant of motion. The systematic drift of the constant of motion in some analyses is attributed to the short simulation time and the size of the lattice. An average run time of 14 hours was observed for ZrB_2 and HfB_2 , with TiB_2 structures taking about 9 hours. The second-order variable wavefunction extrapolation, detailed in [1] was found to speed up calculations without appreciably altering results.

The results of these simulations were first post-processed in *mdtep*, a code by David Quigley, which outputs the cell parameters and energy data from the .md file of a run. This data was then downloaded into MATLAB for post-processing. The average lattice parameters and thermal expansion coefficients were automatically produced with this code. The results are given in the next chapter.

The newly constructed lattices were then deformed by the finite strain technique with linear fitting of the strain patterns as in [47]. Two strain patterns with four strain amplitudes, with a maximum strain amplitude of 0.002, each were used to characterize the elastic state [48]. The elastic constants analysis forces symmetry to be broken while straining, so re-minimization to the Born-Oppenheimer surface is done at each step in the straining cycle [48] with an SCF cutoff of 240 eV/atom. A finer SCF tolerance forces the analysis to diverge, so it becomes necessary to adjust the strain patterns either by reducing the strain amplitudes, or relaxing the SCF tolerance.

The energy was calculated after applying the strain patterns on the lattice and the change in observed energy was obtained with numerical differentiation of equation (4.10). These values were generated automatically from the numerical differentiation and scattered into a table, found in the output file for the analysis. The results of the elastic constants analysis are presented in the next chapter.

5.4 Conclusion

This chapter provided the parameters for each geometry optimization, energy, MD, and elastic constants analysis done on the diborides. The parameters selected were first implemented from the literature [48] and were later refined to optimize runtime. The simulation time was only 0.5 ps for the diborides, although it was increased for the HfB_2 and TiB_2 simulations. The elastic constants simulations were performed using the averaged lattice parameters from the MD simulations using the finite strain approach. The next chapter presents the results obtained using the outlined methodology.

Chapter 6

Findings and Discussions

This chapter presents the results of the ab-initio simulations for the group IV diborides. The resulting elastic constants are compared with Okamoto’s experimental findings (shown in figure 6.1 and ground state properties are verified with other DFT studies. A discussion of the temperature and pressure fluctuations during analysis is provided along with an in-depth discussion of lattice fluctuation during the MD runs. Only a few figures are reproduced in this chapter, with the complete figures relegated to an appendix.

6.1 Results for the ZrB₂ Lattice

The initial NPT results for ZrB₂ showed remarkable consistency with Okamoto’s data [63, 62]. Temperature fluctuations for most of the simulations were very high with the default Nosé mass chosen by CASTEP, as shown in figure 6.2.

Following Nosé [60], the fluctuations of the temperature are expected to have a standard deviation proportional to $\sqrt{N_f}$ where N_f is the number of degrees of freedom in the system:

$$\sigma(T_{instant}) = T \sqrt{\frac{2}{N_f}}. \quad (6.1)$$

There are a total of 10 atoms in the conventional unit cell used for the simulation (in three

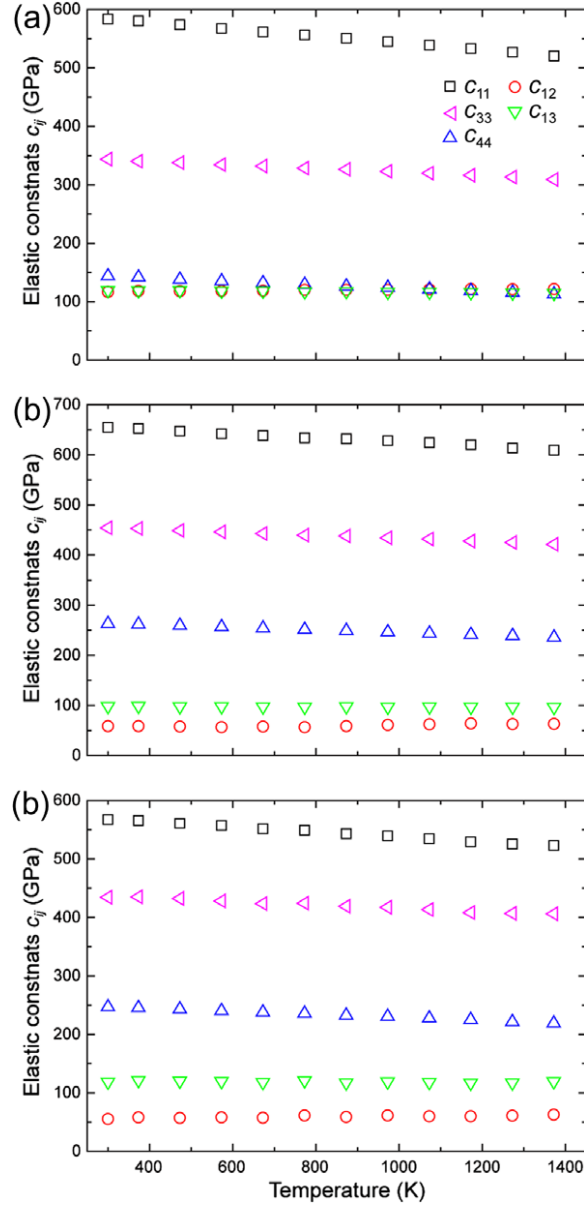


Figure 6.1: The data from Okamoto's recent work [62].

Cartesian directions) for a total of 30 degrees of freedom. For the 2000 K simulation, this amounts to a standard deviation of 516 K. The standard deviations of these fluctuations are similar to those determined from the sample standard deviation function in MATLAB and differ by about 0.6%. Adjusting the Nosé-Hoover mass decreases temperature fluctuations, as revealed in figure 6.3.

Pressure fluctuations are mitigated by setting a higher cell relaxation time (cell time

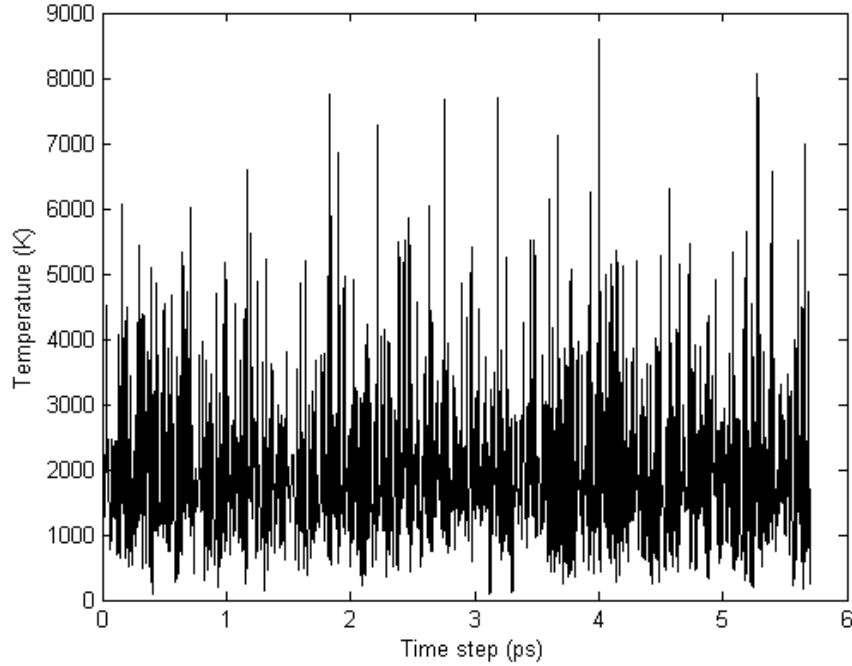


Figure 6.2: Temperature fluctuations for the 2000 K ZrB_2 simulation are high when the Nosé q-ratio is set to 1.0. However, this temperature equals 2000 K on taking the ensemble average. The standard deviation is predicted by formula (6.1).

constant). This forces a longer time for the cell to relax in response to an external pressure, thus reducing local pressure fluctuations. The pressure is controlled by the cell volume with the Andersen Barostat, so a longer relaxation time produces lower fluctuations. Figures 6.4 and 6.5 show the pressure fluctuations for a room temperature simulation and a 1273 K simulation. The pressure fluctuations are naturally higher for the higher temperature due to greater lattice fluctuations. Spurious fluctuations are reduced with a greater cell relaxation time.

The modification of the Nosé-Hoover parameters as mentioned in chapter 5 lowered the temperature fluctuations significantly, as revealed in figure 6.3. Pressure fluctuations are controlled with the lattice time constant parameter in the Andersen barostat. We recall that the Andersen barostat was used so that only isotropic fluctuations in the lattice parameters were permitted when adjusting cell volume. The cell relaxation time controls local fluctuations with time of the pressure by allowing the cell to relax into an equilibrium state,

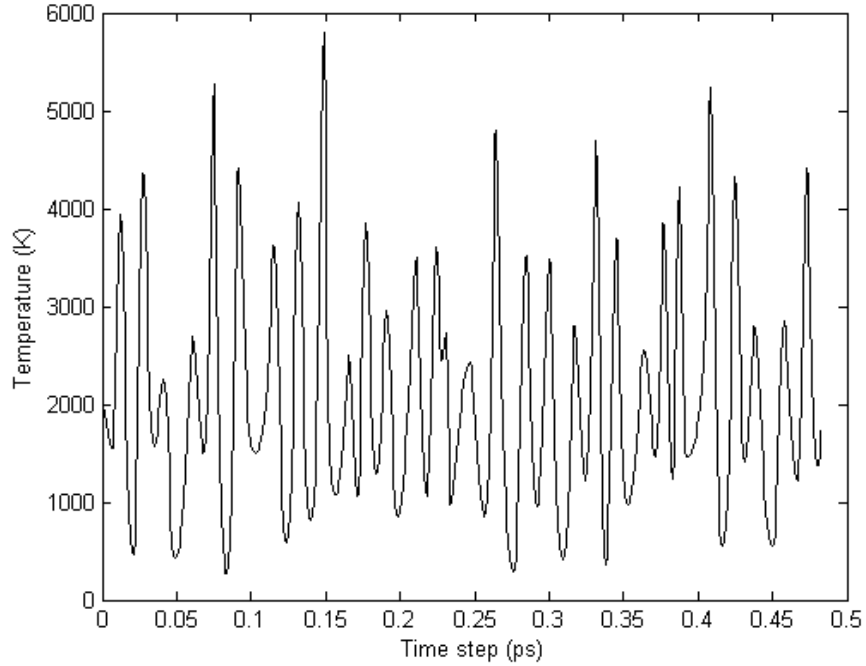


Figure 6.3: Temperature fluctuations for the 2000 K ZrB_2 simulation decrease when adjusting the Nosé-Hoover mass accordingly. The standard deviation is unchanged, however.

i.e. the cell volume adjusts so that the atmospheric pressure condition is established. The time constant serves as a fictitious mass which applies hydrostatic pressure to equilibrate the lattice pressure. Figure 6.5 shows the pressure fluctuation for a 2000 K simulation of ZrB_2 with an increased cell time constant.

Energy conservation is ensured with proper time stepping and thermostating. The Nosé-Hoover thermostat was proven to reproduce the canonical ensemble (NVT) [61, 60] automatically; likewise with the Andersen-Hoover barostat [27]. The ensemble Hamiltonian serves as a constant of motion for the simulation and should show controlled oscillations about a well-defined mean. In some cases, the ensemble Hamiltonian should not vary at all during the simulations. Figure 6.6 shows a typical diverging Hamiltonian for the NPT ensemble for the 1673 K simulation. The fluctuations of the NPT Hamiltonian are decreased with decreased time step and modified thermostating parameters, as shown in figure 6.7 for a higher temperature simulation (2000 K).

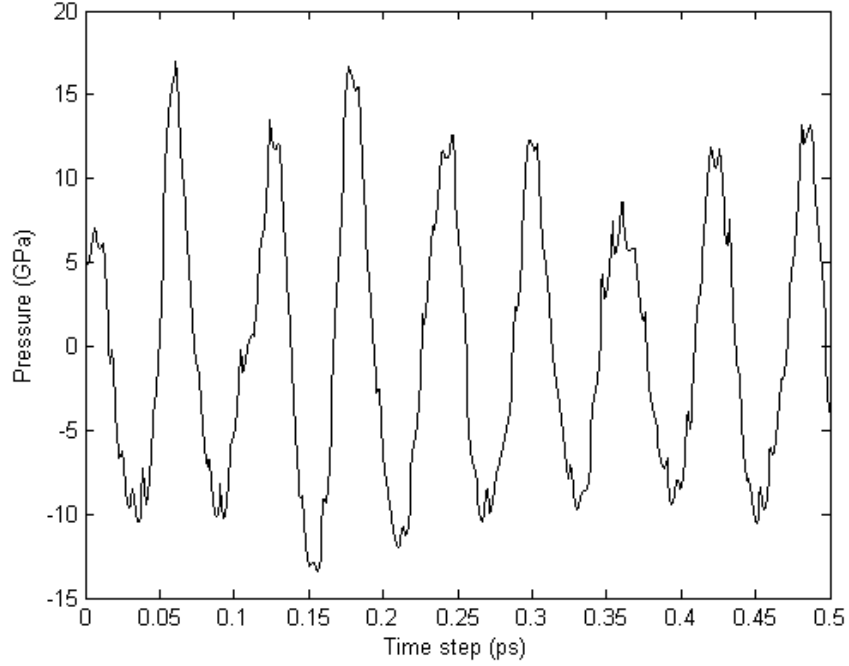


Figure 6.4: Pressure fluctuations for a 273 K ZrB_2 simulation are stable between about ± 15 GPa. Lower pressure fluctuations are expected for larger supercell simulations.

Conservation of energy and stable lattice fluctuations were used to determine the correct lattice parameters for the high temperature simulations. The lattice parameter variations were allowed to become stable before obtaining ensemble averages. The lattice parameter variation for the room temperature simulation is shown in figure 6.8. Similar lattice parameters were obtained for the other temperatures. The fluctuation began to grow at 1673 K, which may be due to the parameter selection for the thermostatting/barostatting or the simulation time. The lattice fluctuations became larger (larger amplitudes) and shifted about a larger mean value as temperature increased. Shorter time steps will reduce fluctuations in the lattice parameter.

Elastic Constants

The monotonic decrease in elasticity is captured well from the simulation data for the temperature range studied by Okamoto. There is a sudden increase in the elastic parameters due

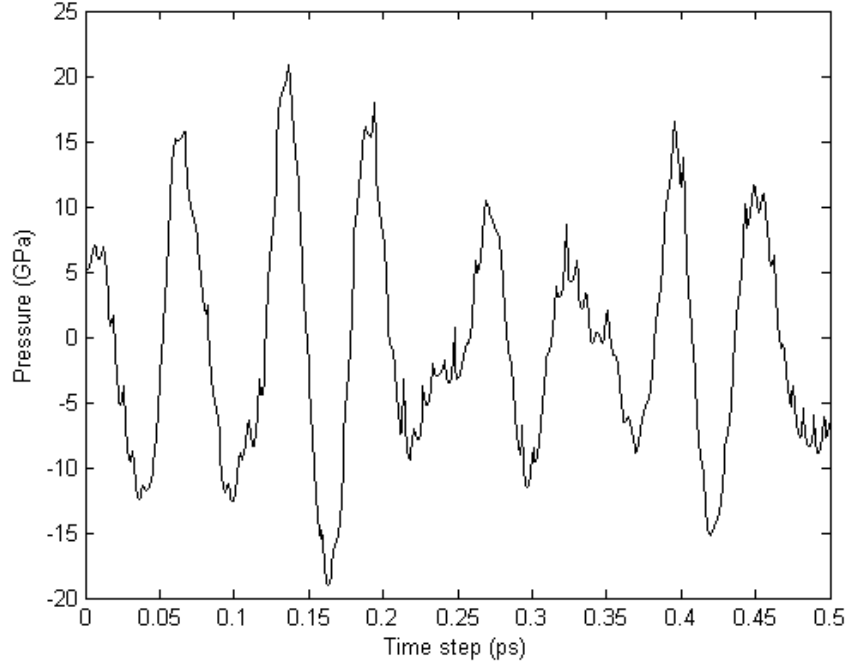


Figure 6.5: Pressure fluctuations are larger for a 1273 K simulation. The period of oscillation is lower due to the greater variation in lattice size (larger lattice fluctuations) at higher temperatures.

to an overrelaxation in the cell. A longer simulation time with an equilibration period could mitigate this deviation. A lower time step with longer cell time constant could also prevent these anomalies. A transition-state search with refined pressure and temperature parameters should be done to explore deviations from the potential energy surface, qualifying potential phase transformations.

Table 6.1 presents the elastic constants for ZrB_2 that were determined through the finite strain approach on reconstructed lattices. These parameters depend solely on the lattice parameters and not the phonon interactions. A linear response analysis is required to investigate the phonon spectra and its effects on the lattice.

The elastic constants as a function of temperature are plotted in figure 6.9. These constants were obtained irrespective of the phonon interactions.

The elastic constants correlate well with Okamoto's original work in the room temperature to 1100°C range. An average deviation of 2.6% is observed between this work and

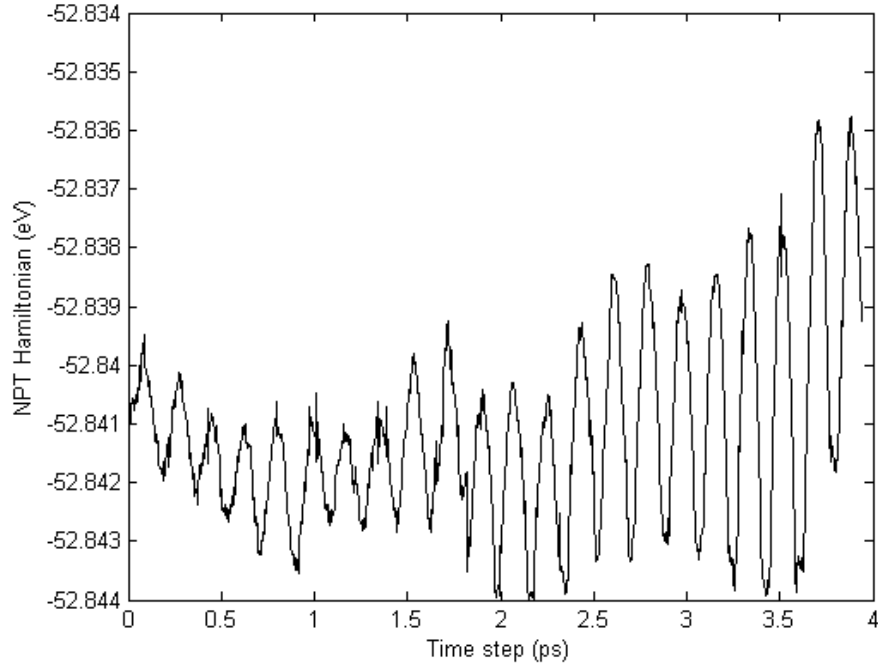


Figure 6.6: NPT Hamiltonian for a 1673 K simulation. The Hamiltonian begins to diverge at around 1.5 ps due to a large time step for the chosen thermostating parameters.

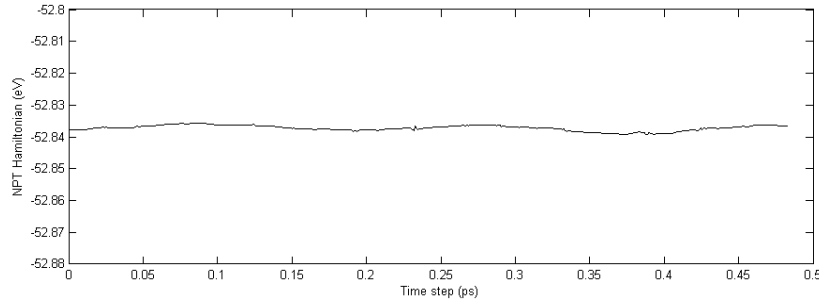


Figure 6.7: The NPT Hamiltonian is nearly constant for the 2000 K simulation for modified thermostat parameters.

Okamoto's data. The simulations underestimate the constants derived by Okamoto due to the underbinding in the GGA already posed by Milman [48].

A longer simulation time with stricter parameters would provide a more accurate representation of the lattice behavior. An ensemble of lattices and a greater (more statistically significant) amount of lattice samplings would eventually converge to the true value of the expanded lattice, without taking phonons or phase transformations into account.

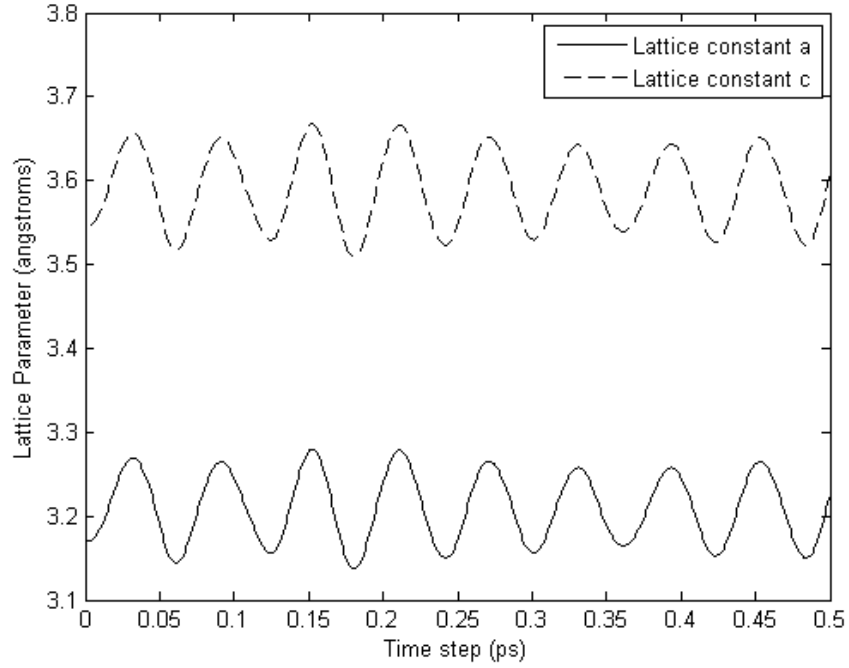


Figure 6.8: Lattice parameter variation for the ZrB_2 lattice at room temperature. These variations, when stable, were used to determine the average lattice parameter for a particular temperature.

An analysis by Pereira et. al [74] showed no solid state phase transitions for pressures up to 50 GPa in ZrB_2 crystals. No recorded solid phase transitions occur for ZrB_2 to the author's knowledge, so the main factors affecting elastic behavior should be the expansion of the lattice and phonon interactions in single crystals.

Milman et. al [48] showed that the periodic unit cell was sufficient in modeling expansion in a lattice by comparison with a 3×3 supercell. The local temperature and pressure fluctuations for our simulated cell are to be expected and are more effectively dampened

Table 6.1: The elastic constants of ZrB_2 at elevated temperatures.

Temperature (K)	C_{11}	C_{12}	C_{13}	C_{33}	C_{44}
273	549.14	57.29	103.38	400.6	249.74
1273	501.9	46.19	88.74	382.5	229.34
1673	508.9	46.5	90.47	384.36	231.7
2000	448.41	28.91	71.67	344.6	213.8
2200	440.13	24.76	71.89	357.63	212.0

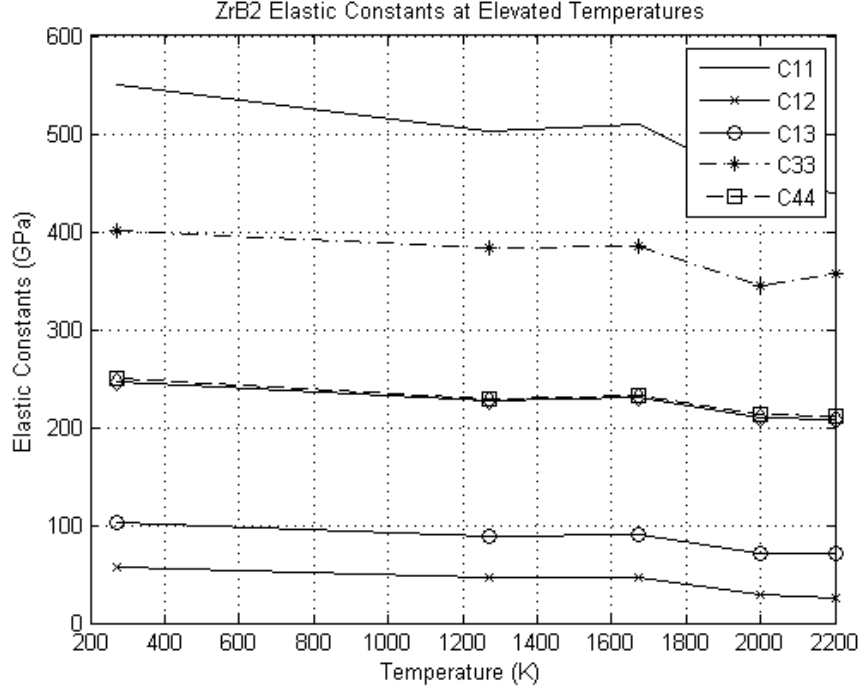


Figure 6.9: The elastic constants of ZrB_2 at elevated temperatures.

with stricter control over the cell time constant and q-ratio.

6.2 Results for the HfB_2 Lattice

The lattice parameter fluctuations were used to gage the stability of the simulation. Ensemble averages were taken once the lattice stabilized about a well-defined mean value. Figure 6.10 shows the lattice parameter fluctuation for a the 2200 K Hf_2 simulation, allowed to run for 0.5 ps. The fluctuations about the mean were used for ensemble averaging for each temperature simulation.

The HfB_2 lattice elastic constants show very good correlation at ground state. The 273 K simulation showed little deviation from the ground state lattice parameters, and so the room temperature elastic constants are comparable to their ground state counterparts recorded in the literature [16].

The elastic constants show a pronounced increase at around 1300 K just like the ZrB_2

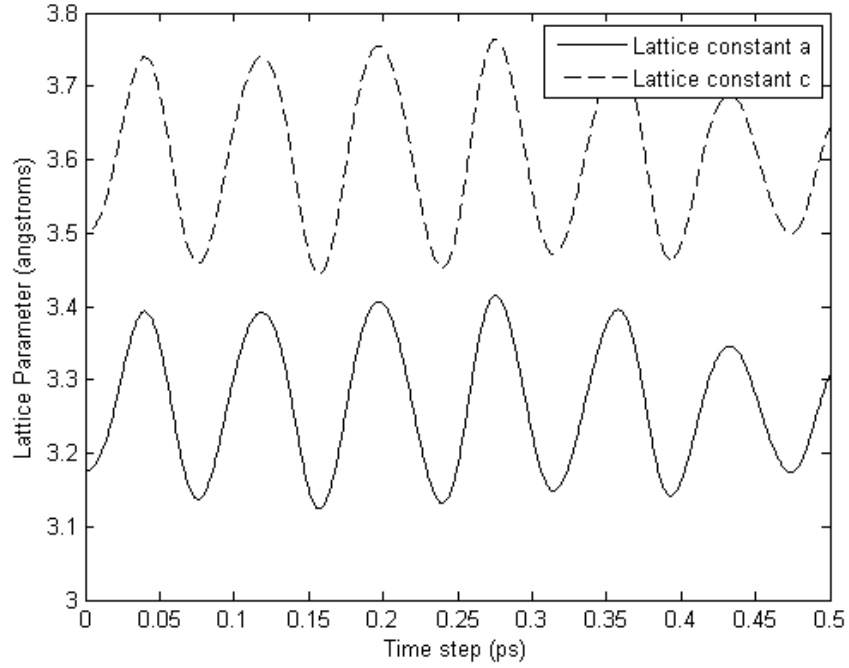


Figure 6.10: Lattice parameter fluctuations for HfB_2 at 2200 K oscillate about a well-defined mean.

structure due to lattice contraction, possibly because of overrelaxation during barostatting. A longer time analysis with a shorter time step should reveal the true parameters. For now, these elastic constants represent a good first order approximation to the elastic behavior at high temperatures, neglecting phonon effects.

To the author's knowledge, there is no experimental data to substantiate these findings. The Okamoto group was the first to present high temperature elastic constants from wave propagation data. However, that study is limited to CrB_2 , ZrB_2 , and TiB_2 .

Table 6.2 and figure 6.11 show the elastic constants for the HfB_2 system. There is again an increase in elasticity observed at around 1300 K, attributed to the simulation time and averaging. A longer simulation time with averaging conducted after equilibration (i.e. sufficiently far away from initial conditions) can provide more accurate results. Again, phonons are neglected in these simulations. However, a consistent correlation with experimental data can raise the question on the importance of the phonon interactions.

Table 6.2: The high-temperature elastic constants of HfB₂ at elevated temperatures

Temperature (K)	C_{11}	C_{12}	C_{13}	C_{33}	C_{44}
273	573	94.42	128.67	449.38	252.8
1273	517.5	76.9	100.98	403.84	229.64
1673	532	81.8	112	414.7	235.5
2000	483.7	66.38	91.81	372.9	213.25
2200	473.17	64.75	86.24	361.17	208.93

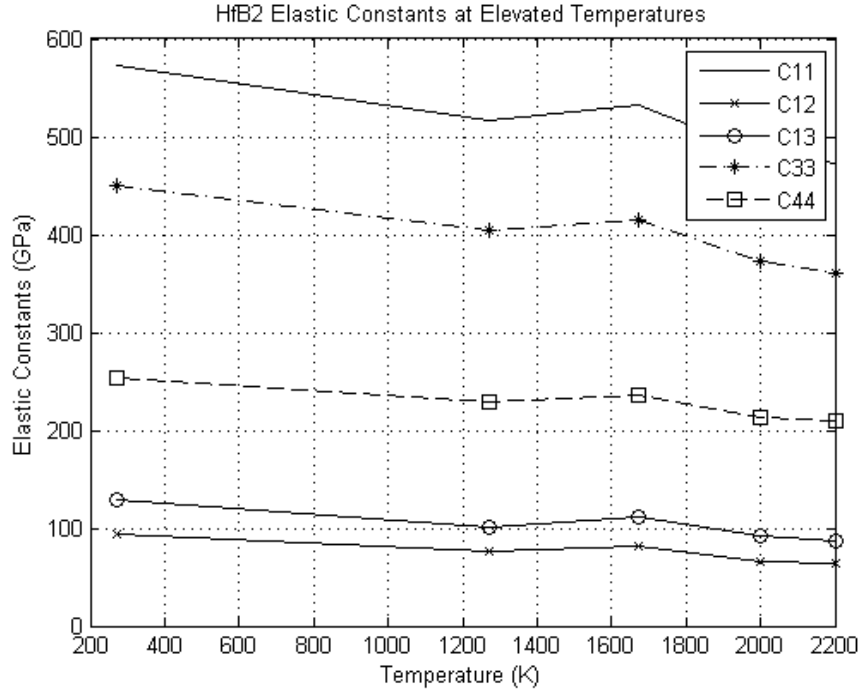


Figure 6.11: The elastic constants of HfB₂ at elevated temperatures.

6.2.1 Supercell

The HfB₂ supercell of figure 5.4 was analyzed at 2200 K for 2.5 ps, with a time step of 0.5 fs, for a total of 5000 steps, as shown in figure 6.13. The lattice fluctuations are similar to those of figure 6.10 and yield a lattice parameter 3.2284 Å. The original run of figure 6.10 yielded a lattice parameter of 3.2311 Å, leading to a relative error of 0.08%.

The supercell was also compared with a 2200 K HfB₂ simulation allowed to run for 10 ps with a 1 fs time step as shown in figure 6.12. The last 3 ps were used to obtain an average lattice parameter of 3.2279 Å, which is remarkably close to the average lattice parameter of

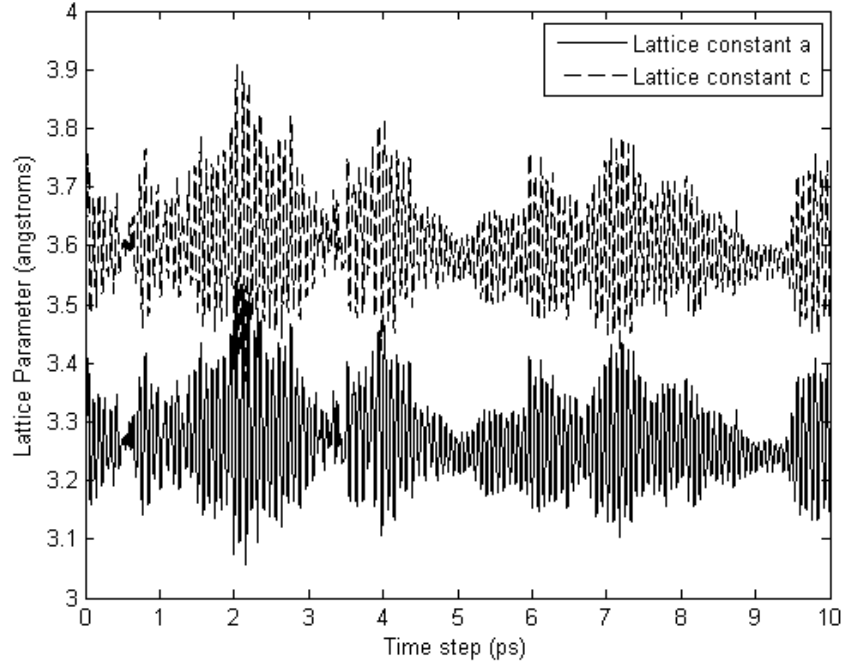


Figure 6.12: Lattice parameter fluctuations for a single HfB_2 unit cell at 2200 K oscillate about a well-defined mean. The oscillations are stable for a simulation time of over 2.5 ps.

the supercell.

The last 3 ps of the 10 ps simulation were used to calculate ensemble averages of the lattice parameter. A final lattice parameter of 3.2247 Å was obtained from the last 3 ps. A full ensemble average of all the time steps showed a lattice parameter of 3.2341 Å, which was the value used for the elastic constants simulation. The lattice parameter predicted for a 1 ps simulation was 3.2331 Å, which shows remarkable correlation with the supercell predicted value. Longer time steps at each temperature value should reveal a similar trend.

6.3 Results for the TiB_2 Lattice

Similar results are expected for TiB_2 with larger elastic constants due to the smaller lattice size and covalent bond strength of Ti with B. The temperature and pressure fluctuations behaved rather well for the TiB_2 simulations, as revealed in figures 6.14 and 6.15.

The elastic constants of TiB_2 are higher than those for HfB_2 and ZrB_2 due to the smaller

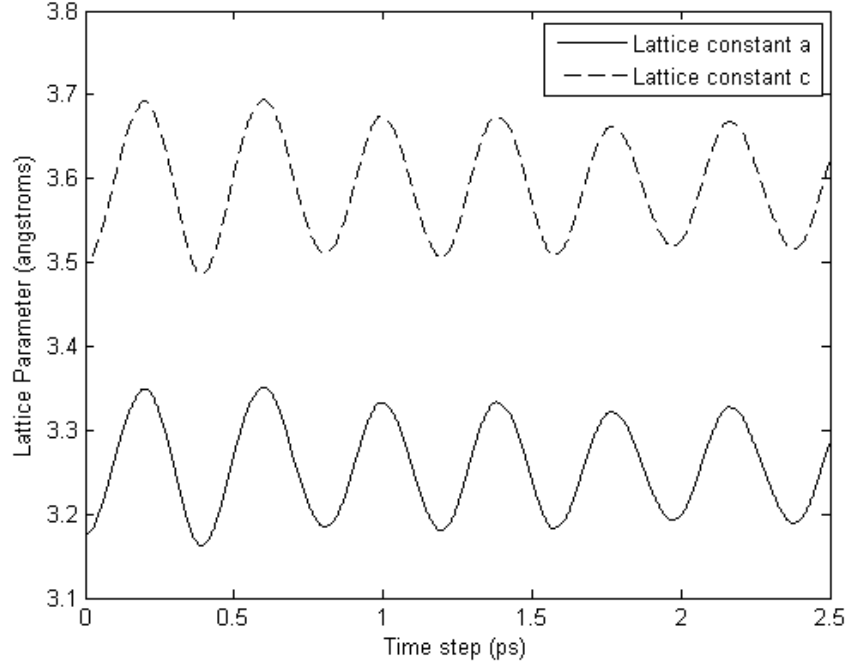


Figure 6.13: Lattice parameter fluctuations for HfB_2 supercell at 2200 K show stable oscillations. The oscillation range is smaller in comparison with figure 6.10. However, the mean value for the lattice parameters is surprisingly close ($\pm 0.3\%$).

lattice parameters. The covalent bonding is stronger in TiB_2 [16] and thus the electronic analysis from the DFT simulations predict shorter lattice fluctuations, as revealed by figure 6.17. Again, these parameters are a lower bound to those of Okamoto because of the underbinding in the GGA. Table 6.3 and figure 6.18 show the results of the elastic constants analysis. No kink in the data is observed, leading to question the validity of the 1673 K simulations for the other diborides. Future work should address this issue.

Table 6.3: The high-temperature elastic constants of TiB_2 at elevated temperatures

Temperature (K)	C_{11}^1	C_{12}	C_{13}	C_{33}	C_{44}
273	637.98	61.6	96.94	469.79	259.51
1273	588.82	51.68	80.89	425.66	239.11
1673	569.46	44.9	71.66	396.36	227.46
2000	553.58	40.9	67.44	388.78	220.5
2200	553.43	40.75	67.6	389.1	220.5

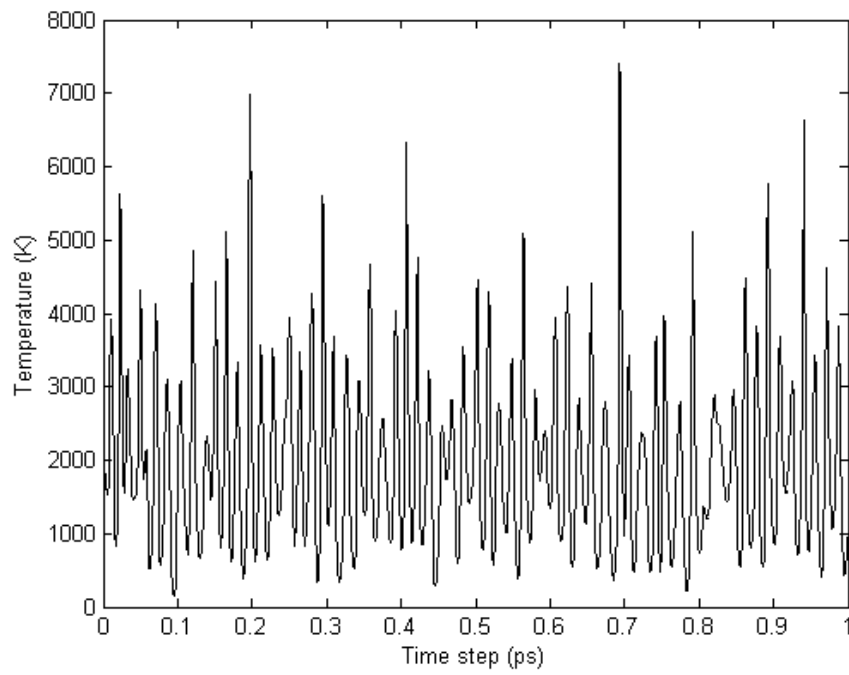


Figure 6.14: The temperature fluctuation for a 2000 K TiB_2 simulation.

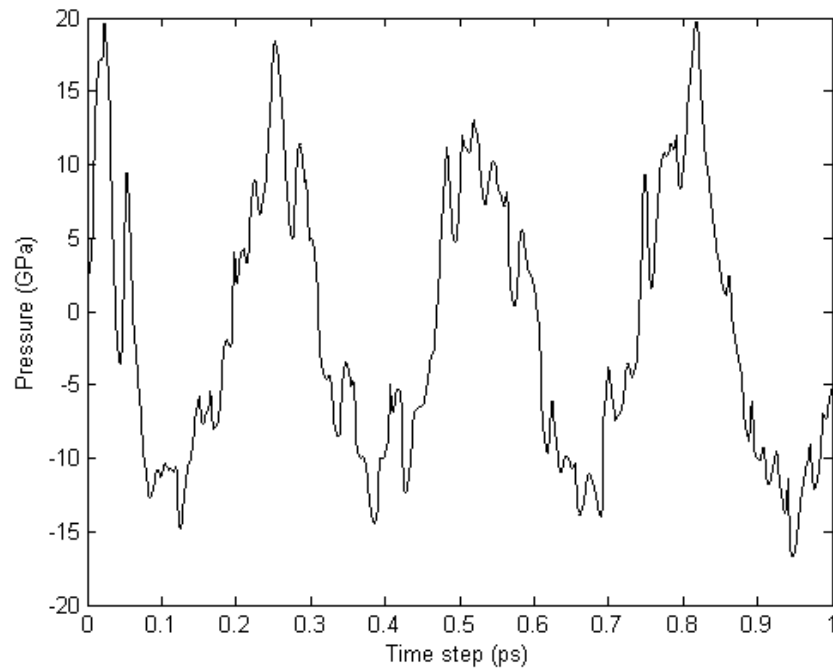


Figure 6.15: Pressure for the 2000 K simulation oscillates between ± 20 GPa.

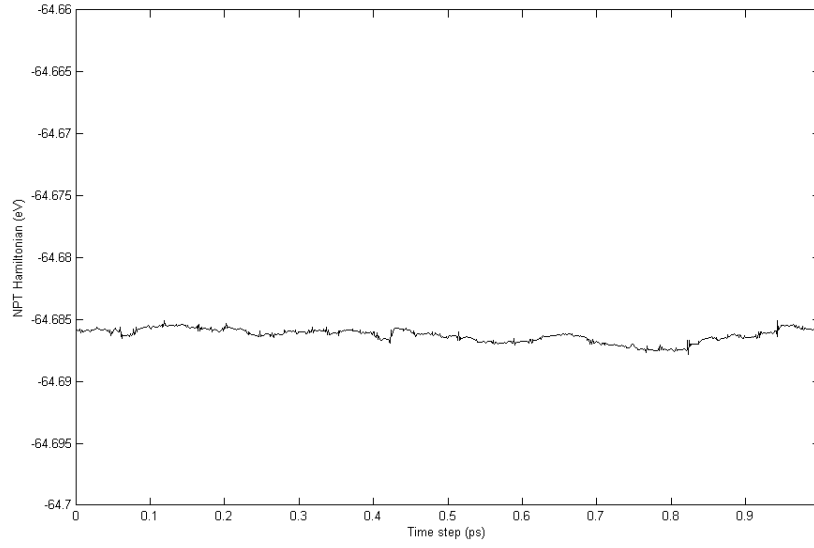


Figure 6.16: The NPT Hamiltonian remained constant about a small range, as expected for conservation of energy.

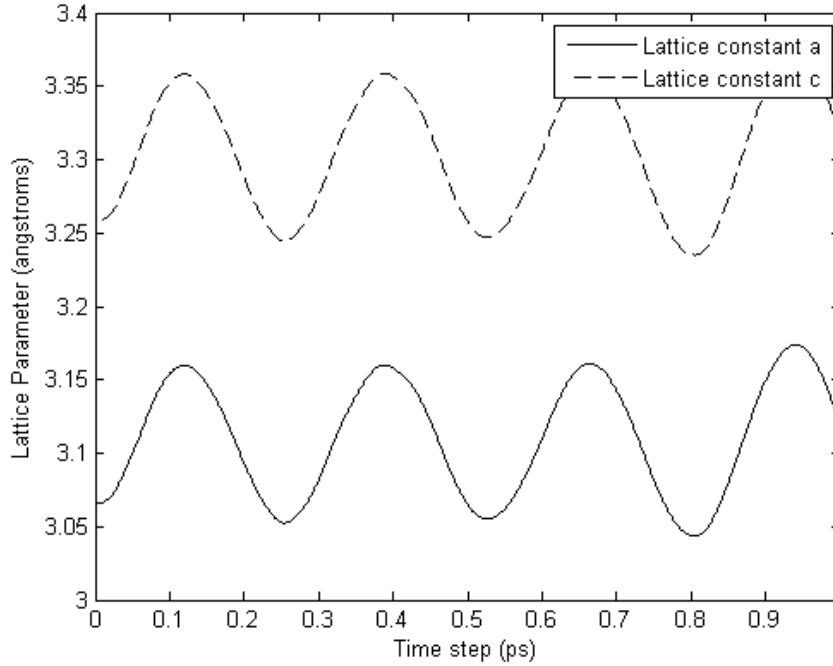


Figure 6.17: The lattice parameters for TiB_2 at 2000 K show shorter fluctuations about a smaller mean value than the ZrB_2 and HfB_2 crystals at the same temperature.

6.4 Summary

The elastic constants at elevated temperatures were determined using ab-initio MD with the DFT approximation for the electronic behavior. The MD analysis was used to update the

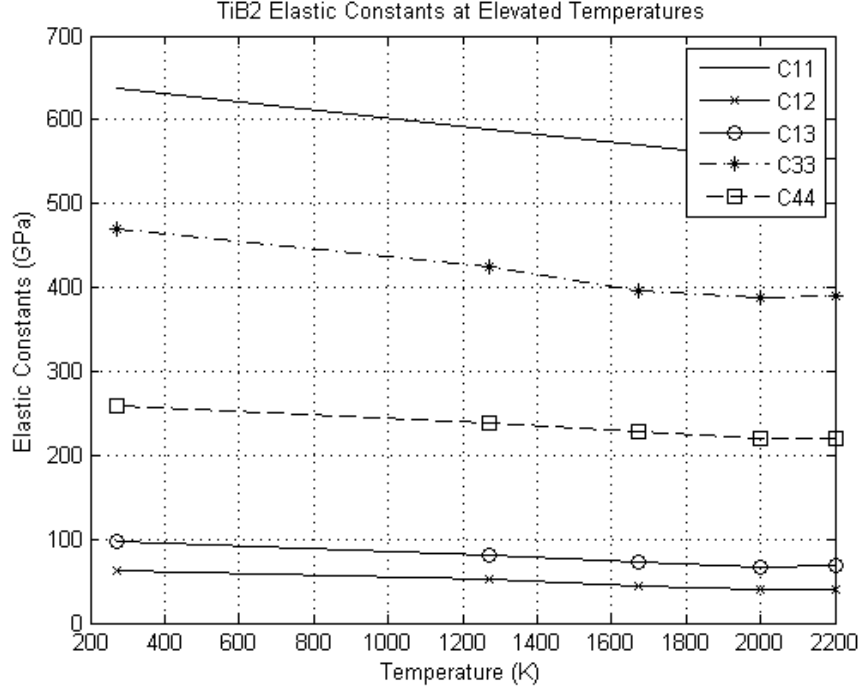


Figure 6.18: The elastic constants of TiB_2 at elevated temperatures. Data shows excellent correlation with Okamoto's work [62] with a clear monotonic decrease in elasticity with increasing temperature. Data is underestimated due to the GGA approximation [48].

trajectories of the individual nuclei after solving the Kohn-Sham equations for the electronic Hamiltonian. The lattice fluctuations for each diboride gave the average lattice parameter for each temperature. The elastic constants analyses revealed the elastic behavior of the diborides without consideration of phonon interactions, and show good correlation with Okamoto's data.

The DFT analysis using the GGA gives a lower bound to Okamoto's data due to the underbinding of the GGA of the electron cloud in occupied orbitals. The LDA, as shown in Mahmud and Islam's work, shows an overbinding, leading to larger elastic constants. The PBE version was selected as a good compromise based on the recommendations from the literature.

The data presented goes beyond Okamoto's experimental work and shows similar monotonic decrease in elasticity, save for a point at around 1673 K in ZrB_2 and HfB_2 . Future work should address this discrepancy by analyzing an ensemble of identically prepared structures

under longer MD analysis times with stricter thermostatting and barostatting.

Chapter 7

Conclusions and future work

This study explored the elastic behavior of group IV diborides using the DFT formalism and ab-initio molecular dynamics simulations. The diborides of Zr, Hf, and Ti show great promise for use in the aerospace industry as coatings for leading edges and as refractory in steelmaking and other industries. A fundamental understanding of the elastic behavior of these materials is essential to evaluating their feasibility in such extreme environments.

Using DFT, single crystal structures of these diborides were constructed and optimized using the PBE version of the generalized gradient approximation (GGA) for the exchange-correlation functionals. The Kohn-Sham equations were solved using an electronic Hamiltonian and the orbitals (i.e. wavefunctions) were computed for the occupied states of these atoms.

These optimized structures were then implemented in an ab-initio MD simulation, where the nuclei behaved as classic point particles under the influence of the electronic potential, which was the expectation value of the Kohn-Sham Hamiltonian. The simulation generated trajectories of the atoms for a specific temperature, thus giving a deterministic picture of the atomic behavior of the lattice from first-principles.

The information from the atomic fluctuations would be used to re-construct the lattice, preserving all symmetry relationships, based on an average lattice parameter. A set of strains

were imposed on the structures and the forces were computed. This gave the stiffness matrix directly by inversion.

This work provided the elastic constants beyond 1300 K, which was the experimental limit for Okamoto's work. These constants correlated well with Okamoto's data and reproduce the monotonic decrease in elasticity well. The computed elastic constants underestimate the values deduced by Okamoto's experimental work. This was attributed to the GGA's underbinding of the electron clouds.

The simulations must now be extended to higher simulation times to explore the energy fluctuations for a fully equilibrium structure. A transition state search must also be conducted to determine any large deviations from the Born-Oppenheimer surface, which could be indicative of a solid-state transformation.

References

- [1] Accelrys Inc. 2003 CASTEP User Guide. (*San Diego, CA: Accelrys Inc.*), 2003.
- [2] A. Bellosi, F. Monteverde, and D. Sciti. Fast densification of ultra-high temperature ceramics by spark plasma sintering. *Int. J. Appl. Ceram. Technol.*, 3(1):32–40, 2006.
- [3] Y. D. Blum and H. Kleebe. Chemical reactivities of hafnium and its derived boride, carbide and nitride compounds at relatively mild temperature. *J. Mat. Sci.*, 39:6023–6042, 2004.
- [4] M. Born. *Z. Physik*, 37:863, 1926.
- [5] M. Born. *Z. Physik*, 38:803, 1926.
- [6] M. Born. *Göttinger Nachr. Math. Phys. Kl.*, page 146, 1926.
- [7] M. Born, W. Heisenberg, and P. Jordan. *Z. Physik*, 35:557, 1926.
- [8] M. Born and J. R. Oppenheimer. On the quantum theory of molecules. *Ann. Physik*, 84(457), 1927.
- [9] S. F. Boys. Electronic wave functions. i. a general method of calculation for the stationary states of any molecular system. *Proceedings of the Royal Society of London. Series A, Mathematical and Physical Sciences*, 200(1063):542–554, 1950.
- [10] A. Chamberlain, W. Fahrenholtz, G. Hilmas, and D. Ellerby. High Strength ZrB₂-Based Ceramics. *J. Am. Ceram. Soc.*, 87(6):1170–2, 2004.

- [11] N. Cho, Z. Bao, and R. F. Speyer. *J. Mat. Res.*, 20(8):2110–2116, 2005.
- [12] A. H. Cottrell. *Theoretical Structural Metallurgy*. Edward Arnold (Publishers) Ltd., 2nd edition, 1955.
- [13] P. A. M. Dirac. *Proc. Roy. Soc. (London). A*, 109:642, 1925.
- [14] P. A. M. Dirac. *Proc. Roy. Soc. (London).*, 123:714, 1929.
- [15] V. A. Epelbaum and M. A. Gurevich. *Zh. Fiz. Khim.*, 32:2274, 1958.
- [16] W. G. Fahrenholtz, G. E. Hilmas, I. G. Talmy, and J. A. Zaykoski. Refractory diborides of zirconium and hafnium. *Journal of the American Ceramic Society*, 90(5):1347–64, 2007.
- [17] J. Fenter. Refractory diborides as engineering materials(Refractory diborides in oxidizing environments, considering mechanical strength, thermal stability, oxidation resistance, heat conductivity, thermal expansion, specific heat and electrical resistance). *SAMPE QUARTERLY*, 2:1–15, 1971.
- [18] M. Ferber, P. Becher, and C. Finch. Effect of microstructure on the properties of TiB₂ ceramics. *Journal of the American Ceramic Society*, 66(1), 2006.
- [19] G. P. Francis and M. C. Payne. Finite basis set corrections to total energy pseudopotential calculations. *J. Phys.: Condens. Matter*, 2:4395–4404, 1990.
- [20] H. Fu, M. Teng, X. Hong, Y. Lu, and T. Gao. Elastic and thermodynamic properties of zrb₂: First principle study. *Physica B: Condensed Matter*, 405(3):846 – 851, 2010.
- [21] H. Goldstein, C. Poole, and J. Safko. *Classical Mechanics*. Pearson, 2000.
- [22] D. J. Griffiths. *Introduction to Quantum Mechanics*. Benjamin Cummings, 2nd.
- [23] J. M. Haile. *Molecular Dynamics Simulation - Elementary Methods*. John-Wiley & Sons, professional paperback ed. edition, 1997.

- [24] P. D. Haynes. *Linear-scaling methods in ab initio quantum-mechanical calculations*. PhD thesis, University of Cambridge, 1998.
- [25] W. Heisenberg. Über den anschulichen Inhalt der quantentheoretischen Kinematik und Mechanik. *Z. Physik*, 43:172–198, 1927.
- [26] P. Hohenberg and W. Kohn. The inhomogeneous electron gas. *Phys. Rev. A*, 31:1695, 1964.
- [27] W. G. Hoover. *Phys. Rev. A*, 31:1695, 1985.
- [28] T. J. R. Hughes. *The Finite Element Method - Linear Static and Dynamic Finite Element Analysis*. Dover Publications, 2000.
- [29] T. A. Jackson, D. R. Eklund, and A. J. Fink. High speed propulsion: Performance advantage of advanced materials. *J. Mater. Sci.*, 39(19):5905–13, 2004.
- [30] D. Jianxin and S. Junlong. Microstructure and mechanical properties of hot-pressed B₄C/TiC/Mo ceramic composites. *Ceramics International*, 35(2):771 – 778, 2009.
- [31] W. B. Johnson, E. Breval, and A. S. Nagelberg. The kinetics of formation of a platelet reinforced ceramic composite prepared by the directed reaction of zirconium with boron carbide. *J. Am. Ceram. Soc.*, 74(9):2093–2101, 1991.
- [32] C. Kittel. *Introduction to Solid State Physics*. Wiley, 8th edition, 2004.
- [33] W. Kohn and L. J. Sham. Self-consistent equations including exchange and correlation effects. *Phys. Rev.*, 140(4A):A1133–A1138, Nov 1965.
- [34] M. Koiwa. *High Temp Mater Proc*, 18:323, 1999.
- [35] K. Laasonen, R. Car, C. Lee, and D. Vanderbilt. *Phys. Rev. B*, 43:6796, 1991.
- [36] K. Laasonen, A. Pasquarello, R. Car, C. Lee, and D. Vanderbilt. *Phys. Rev. B*, 47:10142, 1993.

- [37] A. Leach. *Molecular Modelling: Principles and Applications*. Prentice-Hall Inc., 2001.
- [38] H. Lee, W. S. Hackenberger, and R. F. Speyer. *J. Am. Ceram. Soc.*, 85(8):2131–2133, 2002.
- [39] H. Lee and R. F. Speyer. *J. Am. Ceram. Soc.*, 86(9):1468–1473, 2003.
- [40] S. R. Levine, E. J. Opila, M. C. Halbig, J. D. Kiser, M. Singh, and J. A. Salem. Evaluation of ultra-high temperature ceramics for aeropropulsion use. *Journal of the European Ceramic Society*, 22(14-15):2757 – 2767, 2002.
- [41] S. T. Mahmud, A. K. M. A. Islam, and F. N. Islam. VB_2 and ZrB_2 : a density functional study. *Journal of Physics: Condensed Matter*, 16(13):2335–2344, 2004.
- [42] G. J. Martyna, M. E. Tuckerman, D. J. Tobias, and M. L. Klein. *J. Phys.: Condens. Matter*, 14:2717, 2002.
- [43] D. Marx and J. Hutter. Ab initio molecular dynamics: theory and implementation. *Modern methods and algorithms of quantum chemistry*, 1:301–449, 2000.
- [44] J. M. Melenk and I. Babuska. The partition of unity finite element method: Basic theory and applications. *Comput. Meths. Appl. Mech. Engrg.*, 139:289–314, 1996.
- [45] V. Milman and M. Warren. Elastic properties of TiB_2 and MgB_2 . *Journal of Physics: Condensed Matter*, 13:5585–5595, 2001.
- [46] V. Milman and M. Warren. Elasticity of hexagonal BeO . *Journal of Physics Condensed Matter*, 13(2):241–252, 2001.
- [47] V. Milman and M. C. Warren. *J. Phys.: Condes. Matter*, 13:5585, 2001.
- [48] V. Milman, B. Winkler, and M. I. J. Probert. Stiffness and thermal expansion of ZrB_2 : an ab initio study. *J. Phys.: Condens. Matter*, 17:2233–41, 2005.

- [49] N. Moës, J. Dolbow, and T. Belytschko. A finite element method for crack growth without remeshing. *International Journal for Numerical Methods in Engineering*, 46(1):131–150, 1999.
- [50] S. Moehr, H. K. Mueller-Buschbaum, Y. Grin, and H. G. von Schnering. *Korrektur Zeitschrift fuer Anorganische und Allgemeine Chemie*, 622:1035–1037, 1996.
- [51] H. J. Monkhorst and J. D. Pack. *Phys. Rev. B*, 13:5188, 1976.
- [52] F. Monteverde. Progress in the fabrication of ultra-high-temperature ceramics: in situ synthesis, microstructure and properties of a reactive hot-pressed HfB_2SiC composite. *Composites Science and Technology*, 65:1869–1879, 2005.
- [53] F. Monteverde and A. Bellosi. Effect of the addition of silicon nitride on sintering behaviour and microstructure of zirconium diboride. *Scripta Materialia*, 46(3):223 – 228, 2002.
- [54] F. Monteverde and A. Bellosi. Efficacy of HfN as sintering aid in the manufacture of ultrahigh-temperature metal diborides-matrix ceramics. *Journal of Materials Research*, 19(12):3576–3585, 2004.
- [55] F. Monteverde and A. Bellosi. Microstructure and properties of an $\text{HfB}_2\text{-SiC}$ composite for ultra high temperature applications. *Advanced Engineering Materials*, 6(5):331–336, 2004.
- [56] C. Mroz. Zirconium diboride. *Am. Ceram. Soc. Bull.*, 73(6):141–2, 1994.
- [57] R. Munro. Material properties of titanium diboride. *Journal of Research of the National Institute of Standards and Technology*, 105(5):709–720, 2000.
- [58] T. Mura. *Micromechanics of Defects in Solids*. Kluwer Academic Publishers, 1991.
- [59] L. E. Murr. *Interfacial Phenomena in Metals and Alloys*. Addison-Wesley, 1975.

- [60] S. Nosé. Constant temperature molecular dynamics methods. *Progress of Theoretical Physics Supplement*, 103:1–46, 1991.
- [61] S. Nosé. *Mol. Phys.*, 81:511, 1984.
- [62] N. L. Okamoto, M. Kusakari, K. Tanaka, H. Inui, and S. Otani. Anisotropic elastic constants and thermal expansivities in monocrystal CrB₂, TiB₂, and ZrB₂. *Acta Materialia*, 58(1):76 – 84, 2010.
- [63] N. L. Okamoto, M. Kusakari, K. Tanaka, H. Inui, M. Yamaguchi, and S. Otani. Temperature dependence of thermal expansion and elastic constants of single crystals of ZrB₂ and the suitability of ZrB₂ as a substrate for GaN film. *Journal of Applied Physics*, 93(1):88–93, 2003.
- [64] M. Opeka, I. Talmy, and J. Zaykoski. Oxidation-based materials selection for 2000 C+ hypersonic aerosurfaces: theoretical considerations and historical experience. *Journal of Materials Science*, 39(19):5887–5904, 2004.
- [65] S. Otani and Y. Ishizawa. Preparation of tib₂ single crystals by the floating zone method. *Journal of Crystal Growth*, 140(3-4):451 – 453, 1994.
- [66] S. Otani and Y. Ishizawa. Preparation of zrb₂ single crystals by the floating zone method. *Journal of Crystal Growth*, 165(3):319 – 322, 1996.
- [67] S. Otani, M. Korsukova, and T. Mitsuhashi. Floating zone growth and high-temperature hardness of NbB₂ and TaB₂ single crystals. *Journal of Crystal Growth*, 194(3):430, 1998.
- [68] R. G. Parr and W. Yang. *Density-Functional Theory of Atoms and Molecules*. Oxford University Press, 1989.
- [69] M. Parrinello and A. Rahman. *J. Phys. (Paris)*, C6:511, 1981.
- [70] L. Pauling and E. B. Wilson Jr. *Introduction to Quantum Mechanics With Applications to Chemistry*. McGraw-Hill, 1935.

- [71] M. C. Payne, M. P. Teter, D. C. Allan, T. A. Arias, and J. D. Joannopoulos. Iterative minimisation techniques for ab initio total-energy calculations: molecular dynamics and conjugate gradients. *Rev. Mod. Phys.*, 64(4):1045–1097, 1992.
- [72] J. P. Perdew, K. Burke, and M. Ernzerhof. *Phys. Rev. Lett.*, 77:3865, 1996.
- [73] J. P. Perdew and Y. Wang. *Phys. Rev. B*, 45:13244, 1992.
- [74] A. S. Pereira, C. A. Perottoni, J. A. H. da Jornada, J. M. Leger, and J. Haines. Compressibility of alB₂-type transition metal diborides. *Journal of Physics: Condensed Matter*, 14(44):10615–10618, 2002.
- [75] H. Petla, E. P. Renova, A. Bronson, J. F. Chessa, and N. Maheswaraiah. A computational analysis of a ZrO₂/SiO₂ scale for a ZrB₂/ZrC/Zr ultrahigh temperature ceramic composite system. *Journal of the European Ceramic Society - In Press*, 2010.
- [76] P. Pulay. Convergence acceleration of iterative sequences. the case of scf iteration. *Chemical Physics Letters*, 73(2):393 – 398, 1980.
- [77] R. E. Reed-Hill and R. Abbaschian. *Physical Metallurgy Principles*. Brooks/Cole, 3rd edition, 1994.
- [78] J. J. Sakurai. *Modern Quantum Mechanics*. Addison-Wesley, 1994.
- [79] D. Sciti, L. Silvestroni, and A. Bellosi. Fabrication and properties of HfB₂-MoSi₂ composites produced by hot pressing and spark plasma sintering. *Journal of Materials Research*, 21(6):1460–1466, 2006.
- [80] M. D. Segall, P. J. D. Lindan, P. M. I. J., C. J. Pickard, P. J. Hasnip, S. J. Clark, and M. C. Payne. 2003 castep user guide. (*San Diego, CA: Accelrys Inc.*, 2003).
- [81] I. Shein and A. Ivanovskii. Elastic properties of mono-and polycrystalline hexagonal AlB₂-like diborides of s, p and d metals from first-principles calculations. *Journal of Physics: Condensed Matter*, 20:415218, 2008.

- [82] D. Sholl and J. A. Steckel. *Density Functional Theory: A Practical Introduction*. Wiley-Interscience, 2009.
- [83] Singh, David J. and Nordström, Lars. *Planewaves, Pseudopotentials, and the LAPW Method*. Springer, 2006.
- [84] J. C. Slater. The theory of complex spectra. *Phys. Rev.*, 34(10):1293–1322, Nov 1929.
- [85] J. C. Slater. A simplification of the hartree-fock method. *Phys. Rev.*, 81:385–390, 1951.
- [86] N. Sukumar, D. Chopp, N. Möes, and T. Belytschko. Modeling holes and inclusions by level sets in the extended finite-element method. *Comput. Methods Appl. Mech. Eng.*, 190:6183–6200, 2001.
- [87] B. T. Sutcliffe. The idea of a potential energy surface. In A. F. Sax, editor, *Potential Energy Surfaces*, volume 71 of *Lecture Notes in Chemistry*. Springer-Verlag, 1999.
- [88] R. Thomson. Production, fabrication, and uses of borides. In R. Freer, editor, *The Physics and Chemistry of Carbides, Nitrides, and Borides*, pages 113–20. Kluwer Academic Publishers, Dordrecht, 1990.
- [89] P. Vajeeston, P. Ravindran, C. Ravi, and R. Asokamani¹. Electronic structure, bonding, and ground-state properties of *AlB₂*-type transition-metal diborides. *Phys. Rev. B*, 63(4):045115, Jan 2001.
- [90] D. M. Van Wie, D. G. J. Drewry, D. E. King, and C. M. Hudson. The hypersonic environment: Required operating conditions and design challenges. *J. Mater. Sci.*, 39(19):5915–24, 2004.
- [91] D. Vanderbilt. *Phys. Rev. B*, 32:8412, 1990.
- [92] W. Wang, Z. Fu, H. Wang, and R. Yuan. Influence of hot pressing sintering temperature and time on microstructure and mechanical properties of *TiB₂* ceramics. *Journal of the European Ceramic Society*, 22(7):1045 – 1049, 2002.

- [93] M. E. White and W. R. Price. Affordable hypersonic missiles for long-range precision strike. *J. Hopkins APL Tech. Digest*, 20(3):415–23, 1999.
- [94] D. E. Wiley, W. R. Manning, and O. Hunter. Elastic Properties of Polycrystalline TiB_2 , ZrB_2 and HfB_2 From Room Temperature to 1300 K. *J. Less-Common Metals*, 18:149–157, 1969.
- [95] E. Wuchina, M. Opeka, S. Causey, K. Buesking, J. Spain, A. Cull, J. Routbort, and F. Guitierrez-Mora. Designing for ultrahigh-temperature applications: The mechanical and thermal properties of HfB_2 , HfC_x , HfN_x and αHf (N). *Journal of Materials Science*, 39(19):5939–5949, 2004.
- [96] Y. Yan, Z. Huang, S. Dong, and J. Dongliang. Pressureless Sintering of High-Density ZrB_2 -SiC Ceramic Composites. *J. Am. Ceram. Soc.*, 89(11):3589–3592, 2006.
- [97] H. Zhang, Y. Yan, Z. Huang, X. Liu, and D. Jiang. Properties of ZrB_2 -SiC Ceramics by Pressureless Sintering. *J. Am. Ceram. Soc.*, 92:1599–1602, 2009.
- [98] S. C. Zhang, G. E. Hilmas, and W. G. Fahrenholtz. Pressureless densification of zirconium diboride with boron carbide additions. *J. Am. Ceram. Soc.*, 89(5):1544–50, 2006.

CURRICULUM VITA

Manny Gonzales was born in El Paso, TX on May 2, 1984. The only son of his mother Leonila Cabrera, Manny attended Alta Vista Elementary for kindergarten and Eastwood Knolls and Eastwood High School for subsequent education. Manny found an appreciation for carpentry in High School and decided to pursue a career in engineering.

Manny was the recipient of the Presidential Excellence Scholarship which propelled him to accept the invitation to study at the University of Texas at El Paso. Inspired by professors Stephen W. Stafford and Juan M. Herrera, he double-majored in Mechanical Engineering and Metallurgical and Materials engineering, graduating Summa Cum Laude in both.

Manny has worked at the W.M. Keck Border Biomedical Research center and at the computational mechanics lab while at UTEP. He worked for three consecutive summers at the Los Alamos National Laboratory on various projects, including composite plates under low-velocity impact and accelerated molecular dynamics methods.

A winner of the National Defense Science and Engineering Graduate (NDSEG) Fellowship and the Georgia Institute of Technology Presidential Fellowship and Goizueta Fellowship, Manny will be attending Georgia Tech for the Fall 2010 semester in the Materials Science and Engineering program, pursuing a PhD degree. Manny hopes to follow in the footsteps of the faculty that have inspired him and join the ranks of the academy, seeking to uphold the values and principles that have allowed science to flourish as it has up to this point.

At the time of this publication, Manny had published six proceedings publications and has three journal publications in press. He currently has an abstract accepted to the 2010 Engineering Mechanics Conference to be held at the University of Southern California.

Manny hopes to return to El Paso, TX at some point in his life and perhaps follow in the footsteps of his mentors, building a failure analysis and prevention firm from the ground up.

Permanent Address:

10104 Sugarberry

El Paso, TX 79925